Remote Sensing of Environment 315 (2024) 114478

Contents lists available at ScienceDirect

Remote Sensing of Environment

journal homepage: www.elsevier.com/locate/rse

Grounding-line retreat of Milne Glacier, Ellesmere Island, Canada over 1966–2023 from satellite, airborne, and ground radar data

Yulia K. Antropova [a,*], Derek Mueller [a], Sergey V. Samsonov [b], Alexander S. Komarov [c], Jérémie Bonneau [d], Anna J. Crawford [e,f]

[a] Department of Geography and Environmental Studies, Carleton University, Ottawa, Ontario, Canada
[b] Canadian Centre for Mapping and Earth Observations, Natural Resources Canada, Ottawa, Ontario, Canada
[c] Data Assimilation and Satellite Meteorology Research Section, Environment and Climate Change Canada, Ottawa, Ontario, Canada
[d] Department of Civil Engineering, The University of British Columbia, Vancouver, British Columbia, Canada
[e] Division of Biological and Environmental Sciences, University of Stirling, Stirling, United Kingdom
[f] School of GeoSciences, University of Edinburgh, Edinburgh, United Kingdom

ARTICLE INFO

Edited by: Menghua Wang

Keywords:
Grounding line
Hinge line
Synthetic aperture radar (SAR)
Ice penetrating radar (IPR)
IceBridge
ERS-1/2
Sentinel-1
RADARSAT constellation Mission (RCM)

ABSTRACT

Milne Glacier is a marine-terminating glacier located on the northern coast of Ellesmere Island in the Canadian High Arctic, a region that has experienced extensive ice-mass loss over the last two decades. Milne Glacier flows into Milne Fiord where it transitions from grounded to floating at its grounding line. The glacier rests on a retrograde slope and is therefore potentially vulnerable to marine ice-sheet instability where enhanced basal melt and grounding-line retreat can trigger further deterioration of the glacier. Glacier changes that occur in the ice flexure zone, which spans from the hinge line, the inland limit of tidal flexure, past the grounding line to the landward limit of hydrostatic equilibrium, are critical for glacier dynamics. In this study, we quantify changes in the Milne Glacier grounding-line position from 1966 to 2023 using satellite, airborne, and ground radar observations. Double difference interferometric analysis of Synthetic Aperture Radar (DDInSAR) images acquired between 1992 and 2023 from European Remote Sensing (ERS-1/2) satellites, Sentinel-1 A/B, and RADARSAT Constellation Mission (RCM) was performed to delineate a timeseries of the hinge line. We used these hinge lines to quantify changes in the grounding-line position as their migration rates are directly correlated. RCM-derived results had the highest spatial resolution (10 m) and the best coherence between 4-day repeat acquisitions, which provided the most continuous and detailed hinge-line delineation across the glacier. We also used airborne and ground-based ice penetrating radar (IPR) data collected between 2014 and 2023 to calculate the normalized bed reflection (NBRP) and internal reflection power (NIRP) coefficients to distinguish between basal returns associated with water versus bed and assess signal attenuation within the ice column. Spatial patterns in NBRP and NIRP coefficients allowed us to reliably separate the floating and grounded parts of Milne Glacier. This alternate way of delineating the grounding line was in good agreement with our satellite-based DDInSAR results. Analysis of historical airborne radar surveys in 1966 and 1981 in conjunction with our more recent NBRP/NIRP analysis revealed a ~3.1 km retreat (or ~55 m yr^{-1}) of the grounding line along the glacier centerline over the past 57 years. DDInSAR analysis provided additional details on this shift across the Milne Glacier. ERS and RCM images acquired in 3 and 4-day repeat cycles, respectively, revealed variability in hinge-line positions. This information allowed us to estimate the landward and seaward bounds, associated with the short-term hinge-line migration, that were used to quantify the grounding-line retreat over years. The grounding line retreat was highly asymmetric with the grounding-line retreating at over twice the average rate near the western margin (124 m yr^{-1}) than at the center (53 m yr^{-1}) of the glacier between 2011 and 2023. The calculated average retreat rates of grounding line showed a close association with changes in the ocean temperatures and subglacial discharge. Our study demonstrated that satellite-based monitoring of the hinge line at high spatiotemporal resolution is crucial to better assess the grounding line short-term positional variability and reliably quantify its long-term retreat. Airborne and ground-based radar observations can provide additional in-situ information to explain changes in the grounding line that affect glacier dynamics and viability.

* Corresponding author.
E-mail address: YuliaAntropova@cmail.carleton.ca (Y.K. Antropova).

https://doi.org/10.1016/j.rse.2024.114478
Received 12 April 2024; Received in revised form 9 August 2024; Accepted 16 October 2024
Available online 30 October 2024

1. Introduction

Atmospheric and oceanic warming is occurring rapidly in the Arctic, and this has profound consequences for the cryosphere (IPCC, 2019). The area of floating ice tongues of marine terminating glaciers on the northern coast of Ellesmere Island in the Canadian High Arctic has reduced by ~73 % between 1906 and 2015 (Mueller et al., 2017). The retreat of marine-terminating glaciers is associated with ice losses resulting from negative surface mass balance, submarine melt and/or ice discharge that, in turn, lead to sea-level rise and calving of icebergs. The Canadian Arctic Archipelago (CAA) was the third largest contributor to sea-level rise (0.17 ± 0.02 mm yr^{-1}, Gardner et al., 2011) after Antarctica and Greenland between 2007 and 2009. The most pronounced ice mass losses were driven by highly negative surface mass balance and were observed on Ellesmere Island, the mostly northerly island of the CAA. Although ice discharge played a minor role in the total ice mass losses in the CAA (Millan et al., 2017; Lenaerts et al., 2013), calving events contributed to areal changes of floating glacier tongues and ice shelves (4.9 % and 42.4 % reduction between 1999 and 2015 respectively) across northern Ellesmere Island (White and Copland, 2018). The icebergs originating from the calving events along the northwestern flank of Ellesmere Island drift southward in the Beaufort Gyre to the Beaufort and Chukchi seas, where they could pose a significant threat to marine transportation and industrial activities as the sea ice-free season lengthens (Barber et al., 2014).

Existing studies show that the complex interplay between glacier calving events, increases in ice velocity, surface ablation, basal melt, vertical ice thinning, and/or retreat of the glacier impacts glacier viability in conditions of climatic and oceanic warming (Benn et al., 2007; Scambos et al., 2004). The viability of a marine-terminating glacier can also be viewed in terms of glacier stability, which is largely determined by bed topography. The stability of a marine-terminating glacier is often considered in terms of the movement of the grounding line, a critical feature where ice detaches from the bed and becomes afloat and free of the friction from contact between the glacier and underlying rock and sediment. This transition zone is an important component of glacier ice dynamics (i.e., how the motion and thickness of glaciers change in time and space) as it influences ice discharge from the grounded part of the glacier (Schoof, 2007). While glacial stability is ultimately dependent on several factors (Sergienko and Wingham, 2022), a glacier resting on a retrograde bed slope (i.e., sloping downwards inland) is potentially vulnerable to marine ice-sheet instability; this positive feedback involves melting and recession of the grounding line due to atmospheric and/or oceanic warming triggering thinning and increasing ice velocity that leads to further grounding-line recession (Schoof, 2007; Weertman, 1974). Grounding-line retreat provides a good indication of ice thinning due to increased ice melt or the dynamic vertical thinning that is associated with enhanced ice discharge (Sykes et al., 2009; Schoof, 2007; Rignot, 1996). Therefore, accurate and continuous monitoring of glacier grounding-line locations is important to assess glacier stability and viability, and to quantify and predict the volume of glacial ice discharging into the ocean.

The grounding line is located underwater and ice, and it moves across space and time, thus, it is challenging to directly observe. Researchers use a variety of methods to determine grounding-line position and ultimately this influences where the grounding line or its proxies are delineated. The boundary between the grounded and floating parts of the glacier can be detected based on the change in glacier surface slope, vertical surface displacement of the floating glacier tongue caused by tides, and detection of either bed or water underlying the ice. Techniques to delineate this boundary may be classified as in-situ or remote, and also as ground-, airborne- or satellite-based. In-situ techniques include tiltmeter measurements of surface slope (e.g., Smith, 1991), static and kinematic Global Navigational Satellite System (GNSS) measurements of tidal flexure (e.g., Le Meur et al., 2014; Fricker et al., 2009; Vaughan, 1995; Horgan and Anandakrishnan, 2006) to determine hinge-line positions (Fig. 1) that mark a landward limit of ice flexure zone (Friedl et al., 2020; Sykes et al., 2009). In-situ underwater vehicle observations (e.g., Schmidt et al., 2023) can directly detect the actual grounding-line position. Aerial and ground-based radar surveys can also be used to delineate grounding lines (e.g., CReSIS, 2016; Narod et al., 1988). In radar surveys, a microwave transmitter sends a signal that propagates through the ice until it encounters the boundary between ice and underlying water or bed. The signal is then reflected back to the surface, where a receiver records the power of return signal and its two-way travel time, which can be used to retrieve information on the ice thickness and detect difference between subsurface materials (e.g., water vs. bed). However, the delineation of grounding lines with the use of this technique is not rigorous as variability in ice properties (e.g., temperature, density, salinity, air pockets, layers) and ice cracks may affect the return signal (e.g., Le Meur et al., 2014; MacGregor et al., 2011). In addition, radar surveys as well as other in-situ techniques are spatially and temporally limited due to their logistical complexity.

Unlike in-situ observations, satellite imagery offers routine monitoring of changes in grounding lines in remote areas at large scales. The most commonly used satellite-based grounding-line detection techniques rely on the delineation of its proxy, the hinge line. Repeat laser altimeter-based (e.g., ICESat in Freer et al., 2023) observations can provide routine monitoring of the hinge-line locations; however, optical laser data are prone to various noise sources originating from sunlight reflections and cloud scattering (Rignot et al., 2011). Synthetic aperture radar (SAR) observations can be acquired under cloudy conditions regardless of weather during both day and night at a high spatial resolution, and, therefore, are widely applied over polar regions to precisely detect hinge-line position (Chen et al., 2023; Hogg et al., 2016; Rignot et al., 2011). Repeat SAR images are used to compute information on surface displacement using the double difference interferometric SAR (DDInSAR) technique. This technique is applied to map hinge-line locations, which are often referred to as grounding lines in the most recent InSAR studies (e.g., Chen et al., 2023; Ciracì et al., 2023; Mohajerani et al., 2021), over vast spatial (e.g., Antarctica's coastline) (Mohajerani et al., 2021; Rignot et al., 2011,) and temporal scales (e.g., 30-year period by Millan et al., 2022).

Studies that compare results on delineation of grounding lines and/or its proxies using different methods report findings that vary from close agreement to dramatic differences in the position of these features. Satellite-based DDInSAR and break-in-slope delineations revealed good agreement for slow-moving glaciers and disagreement of up to >100 km for fast-moving glaciers and ice streams (Rignot et al., 2011). The satellite-derived locations which were based on break-in-slope method from optical imagery and/or laser altimetry (Bindschadler et al., 2011a, 2011b; Scambos et al., 2004) were delineated significantly further inland than locations obtained with the use of hydrostatic and tidal methods. The latter methods demonstrated a close agreement within ~1 km (Le Meur et al., 2014). The DDInSAR-derived surface displacements used for hinge line delineations were also in concurrence with modelled tides (Rignot et al., 2024).

Recent studies demonstrate that the hinge line migrates substantially landward (Fig. 1 a) and seaward (Fig. 1 b) with tides, however, this migration and tides can be asynchronous due to bed properties (i.e., hard bed or deformable soft bed) and/or water intrusions in cavities (Rignot et al., 2014; Chen et al., 2023; Freer et al., 2023). Therefore, additional in-situ information, other than tidal changes, is required to better understand the grounding-line migration process obtained with DDInSAR technique. There is a lack of direct and explicit comparison of in-situ radar datasets and satellite DDInSAR-derived results that consider the short-term migration of the hinge line and define bounds of this migration zone. Hereafter the hinge-line migration zone is referred to as landward (HL_{LW}) and seaward (HL_{SW}) bounds of hinge-line migration (Fig. 1 c) but it also was referred to as grounding zone in the recent InSAR-based studies (e.g., Chen et al., 2023; Ciracì et al., 2023; Mohajerani et al., 2021).This study aims to address this gap in the

comparison through a comprehensive analysis of satellite and ground-based radar data collected during three years on Milne Glacier (82°31′N, 80°38′W), a marine-terminating glacier with a floating ice tongue located on the northern coast of Ellesmere Island in the Canadian Arctic Archipelago (Fig. 2 a).

Milne Glacier used to be the principal source of the Milne Ice Shelf (MIS) (Fig. 2b), which resembled a 'classical' ice shelf formed by outlet glaciers or ice streams that flow into a large embayment (Dowdeswell and Jeffries, 2017). This type of system is common in the Antarctic but unique among the Arctic ice shelves that fringe the north coast of Ellesmere Island (Nunavut, Canada), which mostly formed up to 5500 years ago from multiyear sea ice that thickened over time due to snow accumulation at the surface and/or ice accretion at the bottom (Dowdeswell and Jeffries, 2017). The cryospheric features along this coast have changed rapidly over the past century and this makes Milne Glacier a valuable analog for the future of small ice shelves in Greenland and Antarctic.

Historically, the transition of Milne Glacier from grounded to floating was determined at the center line of the glacier based on two airborne radar surveys acquired in 1966 and 1981 (Narod et al., 1988; Hattersley-Smith, 1969) but has never been mapped across the glacier. These radar surveys also demonstrated that Milne Glacier rested on a retrograde slope near its grounding line, and, hence, it is potentially prone to marine ice sheet instability and grounding-line retreat. Precise quantitative information on grounding-line (or its proxy) position and its dynamics from both SAR and radar observations is critical for the analysis of glacier changes. Therefore, this study also aims to delineate a continuous hinge line across Milne Glacier for the first time and use it as a proxy to explore the change in grounding-line position between 1966 and 2023 taking into account its short-term migration.

The objectives of this study are the:

- delineation of the Milne Glacier hinge line based on satellite SAR images acquired by three different SAR platforms between 1992 and 2023;
- detection of the Milne Glacier grounding line using airborne and ground-based ice penetrating radar (IPR) observations acquired between 2014 and 2023;
- validation of DDInSAR-derived HL_{LW} – HL_{SW} bounds of hinge-line migration with grounding-line positions derived from IPR;
- quantification of changes in the Milne Glacier grounding line over 1966–2023 using historical (1966 and 1981) and recent radar observations (2014–2023), and DDInSAR-derived results (1992-2023).

2. Study site description

Milne Glacier is part of the Northern Ellesmere Icefield (unofficial name), which has experienced extensive loss of ice in recent decades (Fig. 2 a). Between 1999 and 2015 this glaciated area decreased by 1705.3 km^2 (~6 % of the initial total area), driven by loss of marine-terminating glaciers with floating ice tongues and ice-shelf systems which were particularly prone to recent climate warming (White and Copland, 2018). After 2010, more than half of the ice discharge from the Northern Ellesmere Icefield was from Yelverton and Milne glaciers (average total of 0.15 ± 0.06 Gt yr^{-1} between 1991 and 2015) (Millan et al., 2017). Using hydrographic observations from 2011 to 2015,

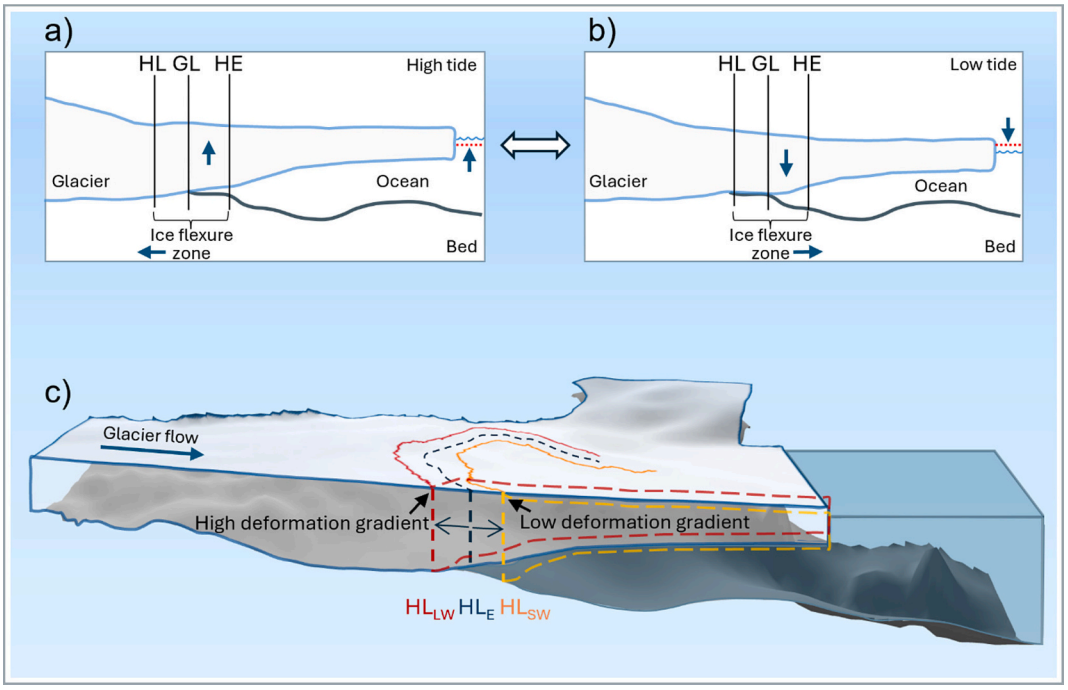

Fig. 1. Schematic illustration of the ice flexure zone, which moves dynamically over the tidal cycle: the hinge line (HL) defines the limit of tidal flexure at the ice surface and marks the landward limit of the ice flexure zone; the grounding line (GL) is the location where ice detaches from the bed and becomes afloat; the hydrostatic equilibrium line (HE) defines where the free-floating part of the glacier tongue begins and marks the seaward limit of the ice flexure zone. (a) At high tide (i.e., the sea surface is above the mean sea level shown with the dotted red line to the right of the glacier tongue), the ice flexure zone (HL, GL, and HE positions) moves landward (b) At low tide, the ice flexure zone moves seaward. (c) Bounds of the landward limit of the ice flexure zone delineated by the most landward (HL_{LW}) and most seaward (HL_{SW}) hinge-line positions associated with high and low absolute values of DDInSAR-derived deformation gradients, respectively. The deformation gradient represents a tide-related ice surface displacement calculated using the DDInSAR technique based on three or four SAR image acquisitions. Assuming there is no sampling bias in the SAR acquisitions, the true average position of the hinge line likely lies between HL_{LW} and HL_{SW} and this can be estimated (HL_E) by calculating the midpoint between HL_{LW} and HL_{SW} This is a more objective way to determine the estimated hinge-line position when multiple interferograms are available, which should lead to a more accurate quantification of the long-term grounding-line retreat. ArcticDEM (Porter et al., 2023) and BedMachine V005 (Morlighem et al., 2020) datasets were used for visualization of the surface and base of Milne Glacier and the bed of the Milne Fiord, respectively. (For interpretation of the references to colour in this figure legend, the reader is referred to the web version of this article.)

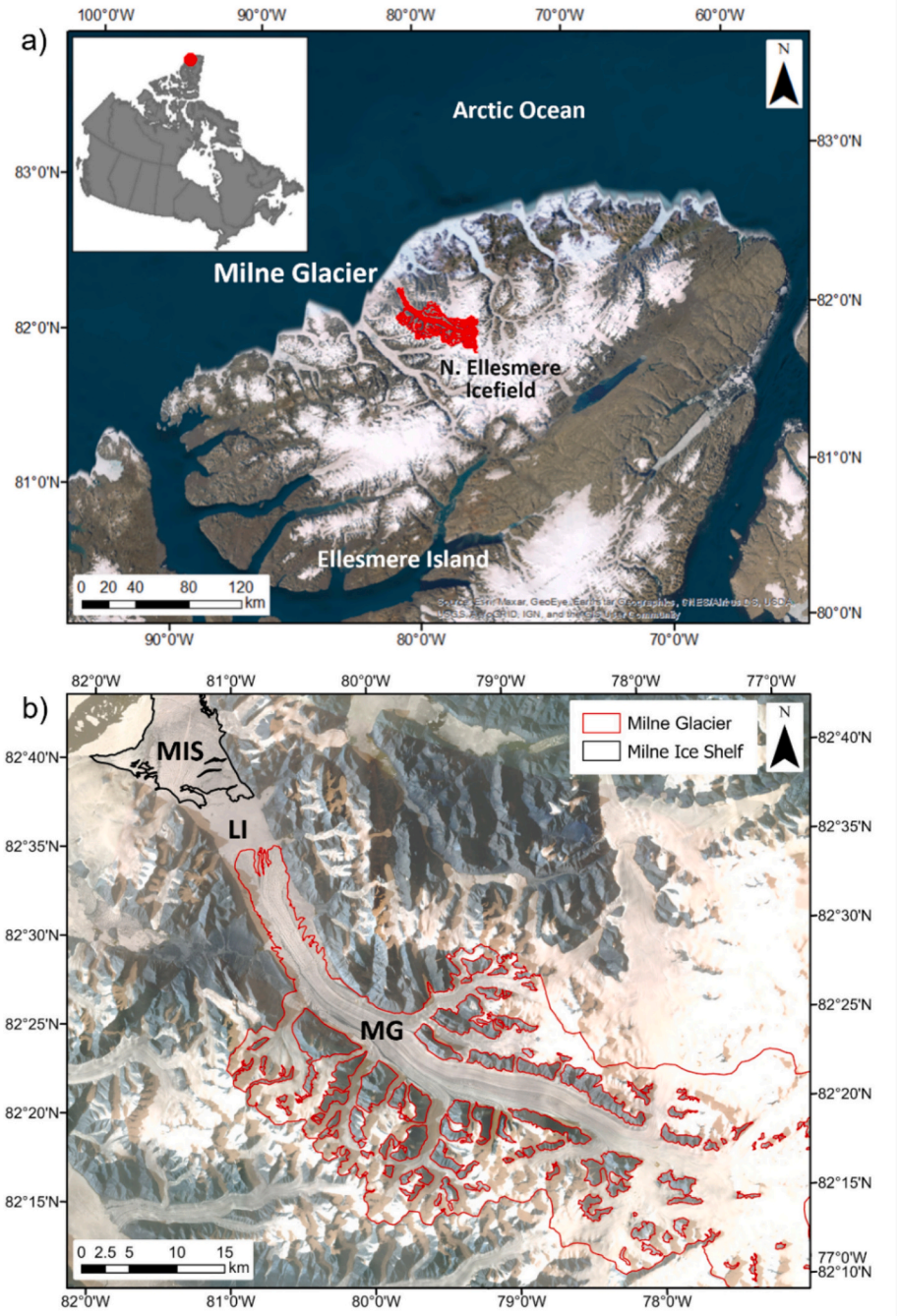

Fig. 2. Study site. (a) Location of Milne Glacier, draining Northern Ellesmere Icefield to Milne Fiord, northern coast of Ellesmere Island, Nunavut; source: ESRI basemap imagery. (b) Milne Fiord glacier system: Milne Glacier (MG) shown with red outline (RGI, 2023), Milne Ice Shelf (MIS) shown with black outline, and 1–3 m thick lake ice (LI) represented by the smooth surface between MG and MIS. The ice features are displayed over a Planet image (Planet Team, 2017) acquired on September 19, 2023. (For interpretation of the references to colour in this figure legend, the reader is referred to the web version of this article.)

Hamilton et al. (2016) calculated submarine melt rate of ~ 4 myr^{-1} at 2.5 km downstream of the Milne Glacier grounding line. The most recent numerical modeling estimates of submarine melt rates at the grounding line vary between 15 and 32 myr^{-1} (Bonneau et al., 2024a).

Jeffries (1984) reported that Milne Glacier flowed into Milne Fiord from an elevation of ~1000 m stretching over ~55 km in a northeast direction and varying in its width from 4 to 5 km. At that time, Milne Glacier was thought to be connected to the MIS, but thin (~3 m) lake ice was present at the eastern and western margins of the glacier tongue, and across the inner part of the MIS adjacent to the glacier tongue. At present, the Milne Glacier tongue is separated by a ~ 1–3 m layer of lake ice from the MIS (Fig. 2 b).

Jeffries (1984) suggested that Milne Glacier was a surge-type glacier given evidence from glacier surface properties such as looped moraines and irregular surface drainage. The terminus advanced by 4.25 km at a rate of ~250 m yr^{-1} between 1966 and 1983, which provided evidence of the variation in the glacier's flow. Mueller et al. (2017) documented substantial changes of the Milne Glacier tongue from 1959 to 2015 based on maps, aerial photos, and satellite images. The glacier tongue advanced between 1959 (extent of 45.4 km^2) and 1988 (extent of 51.5

km^2) and then reached its maximum extent of 61.2 km^2 in 2006. Between 2009 and 2011 the glacier tongue broke away from the glacier through rifting near the grounding line (Mueller et al., 2017). Since then, the Milne Glacier tongue has re-advanced and its extent was 2.9 km^2 in 2015. Ice fragments, separated from the glacier tongue, have been breaking apart, but have been largely kept in place by the presence of lake ice and MIS (Fig. 2 b).

The MIS experienced a minor calving event (~27 km^2) at its northern flank between 1959 and 1963 (Jeffries, 1986; Mueller et al., 2017). Mortimer et al. (2012) reported that the MIS area decreased by 82 ± 8.4 km^2 (29 %) between 1950 and 2009 due to losses from the calving event, the epishelf lake (i.e., a layer of fresh water impounded by an ice shelf that overlies seawater) formation between the MIS and the glacier terminus, and increasing area of ice-marginal lakes between the MIS and the sidewalls of the Milne Fiord. The ice shelf volume decreased by 13 % (1.5 ± 0.73 km^3 water equivalent) between 1981 and 2009. In 2020, a ~ 80 km^2 (43 % of the remaining ice shelf area) ice island separated from the MIS and subsequently drifted into the Arctic Ocean (Bonneau et al., 2021, 2024b). These ongoing changes to the MIS suggest that the ice shelf is not in equilibrium with the current climate and, thus, it is susceptible to disintegration. Given the buttressing role of the ice shelf and lake ice for the Milne Glacier, the changes to the MIS are pertinent to the persistence of the glacier tongue and future glacier-specific ice dynamics. Milne Glacier experienced a slowdown in speed between the early 1990s to 2005, and then accelerated between 2005 and 2020 (Van Wychen et al., 2020; Millan et al., 2017). Although Milne Glacier was thought to be a surging glacier (Jeffries, 1984), a recent study (Van Wychen et al., 2020) argued that it is a pulse-type glacier since its most pronounced changes in flow speed are restricted to the region associated with the ice flexure zone, where the glacier is grounded below sea level (Narod, 1988). The glacier velocity near the ice flexure varied from ~20 m yr^{-1} to ~160 m yr^{-1} between 2011 and 2020. The velocity was between ~100 m yr^{-1} and ~160 m yr^{-1} between 2016 and 2020 in this zone. Therefore, the Milne Glacier's ice flexure zone is associated with pronounced recent changes in ice velocity, so tracking concomitant changes in grounding-line position over this time is required to better understand the glacier dynamics and deterioration processes.

3. Data and methods

Our study used three types of radar datasets over 1966–2023: ground-based and airborne data for grounding-line detection, and satellite observations for hinge-line delineation (Fig. 3).

All datasets were employed to quantify the grounding-line retreat over the last 57 years and examine the agreement between our results for the concurrent years. Detailed descriptions of our datasets and methods used to analyze them are provided in the following sections.

3.1. DDInSAR technique for hinge-line delineation

Marine-terminating glaciers flow downhill under the influence of gravity and advect out over the ocean. The part of the glacier that is located down-glacier of the hinge line also moves vertically due to the ocean tides, while up-glacier of the hinge line this vertical motion does not occur. This physical phenomenon underpins the use of DDInSAR technique to locate the hinge line.

Here, we employed the DDInSAR method (Rignot, 1996) that is commonly used for hinge-line delineation (e.g., Mohajerani et al., 2021; Han and Lee, 2014; Rignot et al., 2011). Differential InSAR computes the differences in the phase between two SAR image acquisitions to compute interferograms and then eliminate the effect of topography, which then reveals information on surface displacement between the acquisitions. The DDInSAR method assumes that the glacier flow does not change substantially between SAR image acquisitions. Therefore, it can be eliminated by computing the difference between two successive interferograms (i.e., double difference interferometry). An interferogram produced by DDInSAR technique shows a dense band of interference fringes at the boundary (i.e., hinge line) associated with ice flexure due to tides as shown in Fig. S1.1. The hinge-line locations can then be digitized manually in geographic information system (GIS) software.

The DDInSAR technique was applied to C-band SAR images acquired between 1992 and 2023 by the following three different satellite systems (Table 1):

1. European Remote Sensing (ERS-1/2) satellite data recorded in 1992 and 2011 as part of dedicated InSAR campaigns,
2. Sentinel-1 (S-1) A/B data acquired yearly between 2017 and 2021, and
3. RADARSAT Constellation Mission (RCM) data acquired in 2023.

Processing of ERS-1/2 and Sentinel-1 images was conducted using GMTSAR, an open-source InSAR software (Sandwell et al., 2011). Inputs for DDInSAR processing included raw SAR images, precise orbital information, and a 30 m resolution ASTER-1 DEM, retrieved for the area of interest with the use of GMTSAR. We compared Sentinel-1 DDInSAR results derived with GMTSAR against DDInSAR products generated by the Alaska Satellite Facility with the use of GAMMA software (Werner et al., 2000) and 30 m resolution GLO-30 Copernicus DEM (Copernicus, 2022). The calculated double difference interferogram results used for hinge-line delineation did not show any pronounced difference in the hinge-line position for the compared Sentinel-1 datasets. Since GMTSAR provided more flexibility in setting processing parameters, including final image resolution, we only analyzed GMTSAR-generated DDInSAR results. The RCM images were processed with GAMMA software with the use of ArcticDEM at 10 m resolution (Porter et al., 2023).

3.2. Grounding-line delineation with ice-penetrating radar

Radar surveys used in this study included three airborne surveys conducted in 1966 (Hattersley-Smith, 1969), 1981 (Narod et al., 1988), and 2014 (CReSIS, 2016) and three in-situ ground-based radar datasets collected on the Milne Glacier in 2018, 2019 and 2023. The grounding-

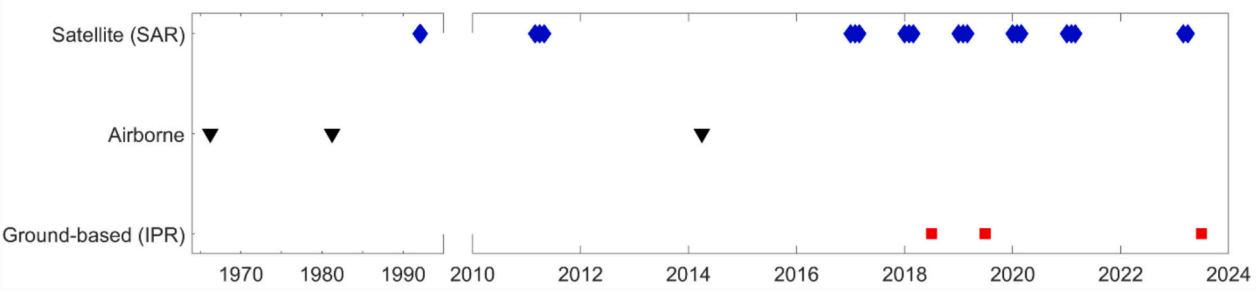

Fig. 3. Acquisition timeline for ground-based (red squares), airborne (black triangles), and satellite radar (blue diamonds) datasets used in this study. (For interpretation of the references to colour in this figure legend, the reader is referred to the web version of this article.)

Table 1
C-band SAR datasets used for DDInSAR hinge-line delineations.

Platform	Beam mode, frame	Polarization	Orbit (ascending or descending)	Time of acquisitions (UTC)	Baseline (days)	Raw image pixel size: range (m) × azimuth (m)	Pixel size of DDInSAR results (m)	N⁰ of hinge lines
ERS-1	Standard (STD), F213	VV	Asc.	1992 (January – March) 00:44	3	26.5 × 19.8	26.9	2
ERS-2	STD, F211	VV	Asc.	2011 (March – May) 00:46	3	26.0 × 19.7	28.1	5
ERS-2	STD, F213	VV	Asc.	2011 (March – May) 00:46	3	26.0 × 19.7	26.9	2
S-1 A/B	Interferometric wide	HH	Des.	2017–2021 (January – March) 13:22	6	2.3 × 13.9	30.2	2, 6, 3, 3, 4
RCM	5 M1	HH	Asc.	2023 (March – April) 19:58	4	1.4 × 2.4	10.0	8

line positions identified from the surveys by Hattersley-Smith (1969) and Narod et al. (1988) were used as a historical baseline to compare against the recent radar datasets collected between 2014 and 2023 (with more details provided in Section 3.3).

The most recent airborne radar dataset was recorded on 1 April 2014 along the centreline of Milne Glacier (Fig. 4) with the MCoRDS 3 radar instrument (Table 2) as a part of NASA's Operation IceBridge campaign. The radar receiver recorded signal amplitude every 33.32 ns, giving 824 records within each of the 3332 radar traces in the dataset. The L1B product, distributed as MATLAB files by CReSIS (2016)), were used in our study. In particular, we used the received power of the radar signal measured in Watts (W) at the ice surface and the ice bottom. The final product has an along-track resolution of about 25 m, a sample spacing of about 14 m, and a depth resolution of 4.5 m (CReSIS, 2016; Paden et al., 2010).

The three most recent ground-based radar datasets (Fig. 4) were collected on the Milne Glacier during our field campaigns in July of 2018, 2019, and 2023. The IPR (Table 2), was developed by Blue Systems Integration Inc. (Mingo and Flowers, 2010). The IPR receiver recorded signal amplitude every 2 ns for 3000 records within every trace. A HiPer V Dual-Frequency GNSS receiver (Topcon Positioning Systems Inc.) was incorporated into the transmitter unit to record precise positional data. The IPR data were collected by towing the IPR unit on skis behind a hiker. The IPR surveys were collected along transects of ~3.5 km, ~7.8 km, and ~6.4 km in 2018, 2019, and 2023, respectively. Each of these transects intersected the assumed grounding-line location. These datasets were processed with the Radar Tools package (v 0.5, Wilson and Mueller, 2023) to identify surface and bottom of the ice and retrieve the associated voltage (V) of the radar signal. These three in-situ datasets had a mean along-track sample spacing of about 5 m. The system resolution Δh (i.e., the minimum distance that can be resolved between two impulses) was calculated using the time interval between the amplitude samples, Δt, and signal propagation speed in ice, c_i (Bogorodsky et al., 1985):

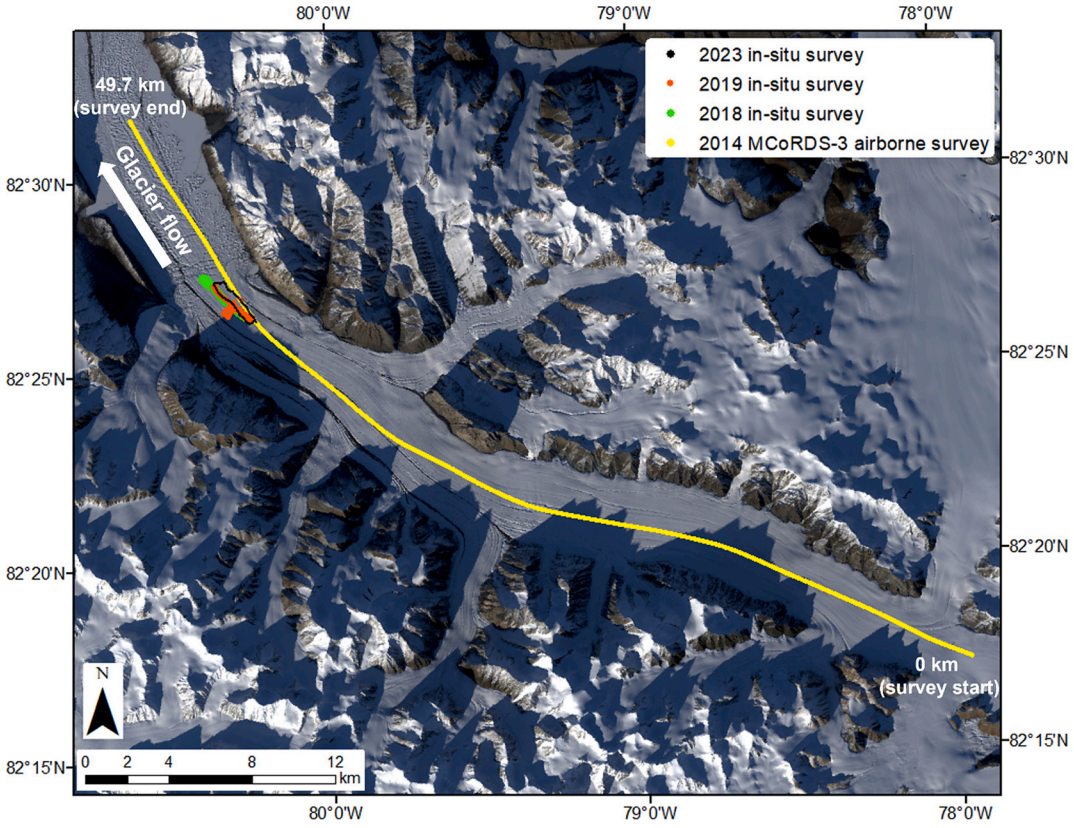

Fig. 4. In-situ airborne and ground-based radar surveys acquired between 2014 and 2023 at Milne Glacier overlayed on a true-colour Landsat-8 image acquired on 13 September 2018.

Table 2
Characteristics of airborne and ground-based radar systems.

System	Frequency (MHz)	Sampling (ns)	GPS receiver	Acquisition elevation/ground offset (m)	Spatial resolution (m)	Depth resolution (m)
MCoRDS 3 radar	180–210	33.32 (824 records per trace)	several GPS and inertial navigation systems used for IceBridge campaign	High-altitude data	along-track: 25 between samples: 14	4.5
Blue Systems radar	25	2 (3000 records per trace)	Topcon HiPer V Dual-Frequency GNSS receiver	0.18	~5	0.17

$$\Delta h = \frac{\Delta t \times c_i}{2} \tag{1}$$

where the signal-propagation speed in ice, c_i, was estimated based on the speed of light in a vacuum, c, (3×10^8 ms^{-1}) with a representative dielectric constant value for ice (ϵ) of 3.15. This assumes a uniform media with no loss, i.e., the imaginary part is zero (Bogorodsky et al., 1985):

$$c_i = \frac{c}{\sqrt{\epsilon}} \tag{2}$$

Thus, the signal propagation speed in ice was 1.69×10^8 m s^{-1}, which yielded a system resolution of 0.17 m.

To characterize sub-ice properties, the bed-reflection power (BRP) and the internal-reflection power (IRP) coefficients (Copland and Sharp, 2001; Gades et al., 2000) were computed from the four radar datasets collected in 2014, 2018, 2019, and 2023. BRP represents the amount of microwave energy reflected from the ice base. Relatively high values of BRP coefficients suggest the existence of water underlying the ice (e.g., floating glacier tongue), while low BRP values indicate rocks and/or sediments under the ice layer (Gades et al., 2000). IRP values were used to qualitatively assess the signal power losses within the ice column and detect patterns along the transect associated with grounded and floating ice. The BRP and IRP coefficients were calculated using the following equations:

$$BRP = \frac{1}{(t_3 - t_2)} \int_{t_2}^{t_3} A^2(t)dt \tag{3}$$

$$IRP = \frac{1}{(t_2 - t_1)} \int_{t_1}^{t_2} A^2(t)dt \tag{4}$$

where $A(t)$ is the signal magnitude at time t, $t_3 - t_2$ is a time window encompassing the bed signal, and $t_2 - t_1$ is a time window encompassing the part of the signal corresponding to the internal structure of the ice. Both BRP and IRP coefficients were normalized with respect to the maximum BRP values in a given radar survey and expressed in dB units as follows:

$$NBRP = 10 \times log_{10} \frac{BRP}{BRP_{max}} \tag{5}$$

$$NIRP = 10 \times log_{10} \frac{IRP}{BRP_{max}} \tag{6}$$

In order to determine the BRP and IRP integral bounds t_1, t_2 and t_3 for a given signal response (power versus time), we introduced an adaptive automated approach that is based on the standard deviations calculated in small sliding time windows along the signal trace, and compared it against a relatively low threshold value computed for a reference time window corresponding to the internal ice layer. This approach is inspired by the fact that the signal standard deviation tends to be relatively large around the peak locations denoting the air/ice and ice/bed transitions, and it tends to be much lower within the ice. The optimum sizes of the sliding time window were chosen based on the visual assessment of the signal traces. For IceBridge radar data, the size of the sliding window was chosen to be 10 sample bins (i.e., 333.2 ns), while for the IPR data, the window size was chosen to be 15 sample bins (i.e., 30 ns).

Following Gades et al. (2000) and Copland and Sharp (2001), we analyzed the effect of ice thickness on BRP and IRP values and found that it was poorly explained by fitting exponential functions (section S2 in the supplementary materials). This result was consistent with the suggestion that the ice temperature and/or variability in bed properties likely have a stronger effect on the changes in the signal than the ice thickness alone (Wilson et al., 2014; Copland and Sharp, 2001). This suggestion was corroborated by our IceBridge radar mean signal trace analysis for the glacier head and terminus that demonstrated much

stronger surface signal attenuation in the floating terminus compared to the grounded part of the glacier. As a result, the radar datasets were not corrected for the effect of the ice thickness, but the transects of the NBRP and NIRP coefficients were analyzed together to detect the patterns associated with grounded (i.e., low BRP values) and floating (high BRP values) parts of the Milne Glacier.

3.3. Comparison of DDInSAR and IPR results and quantification of the grounding-line retreat between 1966 and 2023

Our DDInSAR-derived hinge-line locations were compared against IPR-derived grounding lines. The grounding lines were mapped along with the landward limit of the ice flexure zone bounded by the landward and seaward hinge-line positions (i.e., HL_{LW} and HL_{SW}) for each year on record. We simulated tides in Milne Fiord to better understand the association between the tidal cycle, the DDInSAR-derived vertical displacements and hinge-line positions (HL_{LW} - HL_{SW}). The sea surface elevation due to tides at the time of SAR acquisitions was estimated using the t-tide algorithm (Pawlowicz et al., 2002). T-tide simulations were based on tidal constituents derived from a 10-month in-situ pressure record from an RBR Duet datalogger moored at ~10 m depth in a lateral bay off the west side Milne Fiord (Fig. S3.1 a) between September 3, 2016 and July 4, 2017. The comparison of these datasets with DDInSAR results confirmed that the most landward hinge-line positions (HL_{LW} bound in Fig. 1) corresponded with the highest absolute values of tide difference between SAR scene acquisition times, while the most seaward DDInSAR hinge-line positions (HL_{SW} bound in Fig. 1) were associated with the lowest absolute values of tide difference (Fig. S3.1 b). Then we examined the agreement between the DDInSAR-derived landward limits of the ice flexure zone (HL_{LW} and HL_{SW} bounds) and IPR-derived grounding-line locations to contextualize the overall agreement between DDInSAR and IPR results across the glacier.

We also quantified the grounding-line retreat over the period of available observations based on the IPR-derived grounding-line results (1966–2023) and DDInSAR-based hinge-line locations (1992-2023). Grounding-line positions in 1966 and 1981 were identified from airborne radio-echo sounding data acquired along the centreline of the Milne Glacier using 35 MHz and 840 MHz radar systems, respectively (Hattersley-Smith, 1969; Narod et al., 1988). Magnetic data tapes that recorded the original data have been lost, so our analysis was conducted from scanned copies of the paper-based maps of the flight track and radargrams. The navigational accuracy for the flight lines surveyed by Hattersley-Smith's (1969) was limited to line-of-sight paths or sun-compass courses based on identifiable landmarks from air-photo mosaics. The flight lines were plotted over the National Topographic System 1:250,000 maps, published by the Surveys and Mapping Branch, Department of Energy, Mines and Resources (currently Natural Resources Canada), Ottawa. The raster image of the Milne Glacier survey over the topographic map (Hattersley-Smith, 1969) was georeferenced using a first-order transformation to a digital version of the identical topographic map (CanMatrix, Natural Resources Canada). The resulting georeferenced map had a resolution of 44 m and a sub-pixel horizontal uncertainty, i.e., the total root-mean square error (RMSE) of 8.5 m. In 1981, the flight track was navigated with the use of an Omega system in combination with dead reckoning and oblique aerial photography. The absolute horizontal accuracy of this navigation system was initially assessed at the level of ~1 km (Prager, 1983) and later was refined to 200–230 m (Narod et al., 1988; Mortimer et al., 2012). The raster scan of the flight map was transformed onto the same map as above with a resolution of 200 m and an RMSE of 172.4 m. The historical datasets were mapped along with the recent grounding-line positions retrieved from radar data collected in 2014, 2018, 2019, and 2023 to quantify the grounding-line retreat along the central line of Milne Glacier in the last 57 years.

The DDInSAR-derived hinge-line positions were used as a proxy for the retreat of the grounding line. Although there are minor differences in the lateral positions across the fiord between the grounding-line and hinge-line locations, elastic beam theory has shown that migration rates of hinge and grounding lines are directly correlated (Rignot, 1996; Hogg et al., 2016). Therefore, the delineation and monitoring of either of them provides an accurate means of assessing grounding-line migration, provided that retreat rates are calculated using a single method.

Since the HL_{LW} – HL_{SW} zone shifts position with short-term changes in sea level, we quantified this in years with more than one observation. Multiple hinge-line positions within a given year were used to identify the HL_{LW} and HL_{SW} bounds (i.e., the most landward and seaward hinge lines, HL_{LW} – HL_{SW}, as shown in Fig. 1) for that year, which provides an upper and lower bound on the hinge-line position due to tidal effects. Hinge-line retreat was quantified by comparing HL_{LW} positions, HL_{SW} positions, and the mean positions (HL_E in Fig. 1 c) between years and then average retreat rates per year over several time periods were computed.

The grounding/hinge-line retreat was assessed using three along-glacier transects representing the glacier's western, central, and eastern parts (shown in Fig. 12 in Section 4.1 along with the results). The western transect was drawn approximately parallel to the glacier's flow, the central transect was delineated along the 1966 flight track, and the eastern transect was outlined parallel to the central transect and close to the 2014 IceBridge track.

The combined IPR and DDInSAR-derived retreat analysis allowed us to compare the grounding-line average retreat rates over several periods between 1966 and 2023. Annual average retreat rates were plotted for comparison within 1966–2023 (IPR-derived retreat), 2011–2023, 2011–2018, and 2018–2023 (DDInSAR-derived retreat rates) periods. Periods with the most comprehensive DDInSAR-derived results (2011, 2018 and 2023 shown in Fig. 6 b, d, and h respectively in Section 4.1) were chosen to reveal the most pronounced variability in hinge-line locations and provide the most complete information on the HL_{LW} – HL_{SW} bounds. This approach may not necessarily reveal the actual extremes for the LW-SW bounds, however, years with the most comprehensive records (i.e., large sample size) were considered providing reliable information about the average retreat rates.

4. Results

4.1. Hinge-line delineation based on satellite DDInSAR analysis

We delineated 35 hinge-line locations over eight years (i.e., 1992, 2011, 2017–2021, and 2023) of SAR observations acquired by three different spaceborne SAR C-band systems. Examples of double-difference interferograms used for delineation of hinge lines for each of the eight years of observations are shown in Fig. 5. ERS images were acquired every 3 days, which was the shortest time interval among all SAR acquisitions. These frequent image acquisitions maintained high coherence between images and provided opportunity for hinge-line delineation across most of the glacier width in 1992 and 2011 (Fig. 5 a-b). Sentinel-1 data with a 6-day time interval between acquisitions provided an opportunity to delineate hinge-line locations for 5 years in a row between 2017 and 2021. However, the longer time span between acquisitions significantly degraded coherence, and the results were noisier compared to ERS-1/2 and RCM. Therefore, with Sentinel-1 data, hinge lines could only be successfully delineated within the central zone of the glacier (Fig. 5 c-g). RCM images with 4-day time intervals between acquisitions provided very good coherence and the opportunity to delineate hinge-line locations from the double-difference interferograms with the finest spatial resolution of 10 m (Fig. 5 c). These datasets had very few incoherent pixels, which allowed eight hinge lines to be delineated across the entire width of the glacier (Fig. S1.1) between 7 March and 24 April 2023. The clear "bull's-eye" pattern was observed downglacier of the hinge lines in the western side of the glacier in 2023 (e.g. Fig. 5 h and Fig. S1.1). This pattern was also visible, although less pronounced, in 2011 (Fig. 5 b). This likely indicates a local grounding of

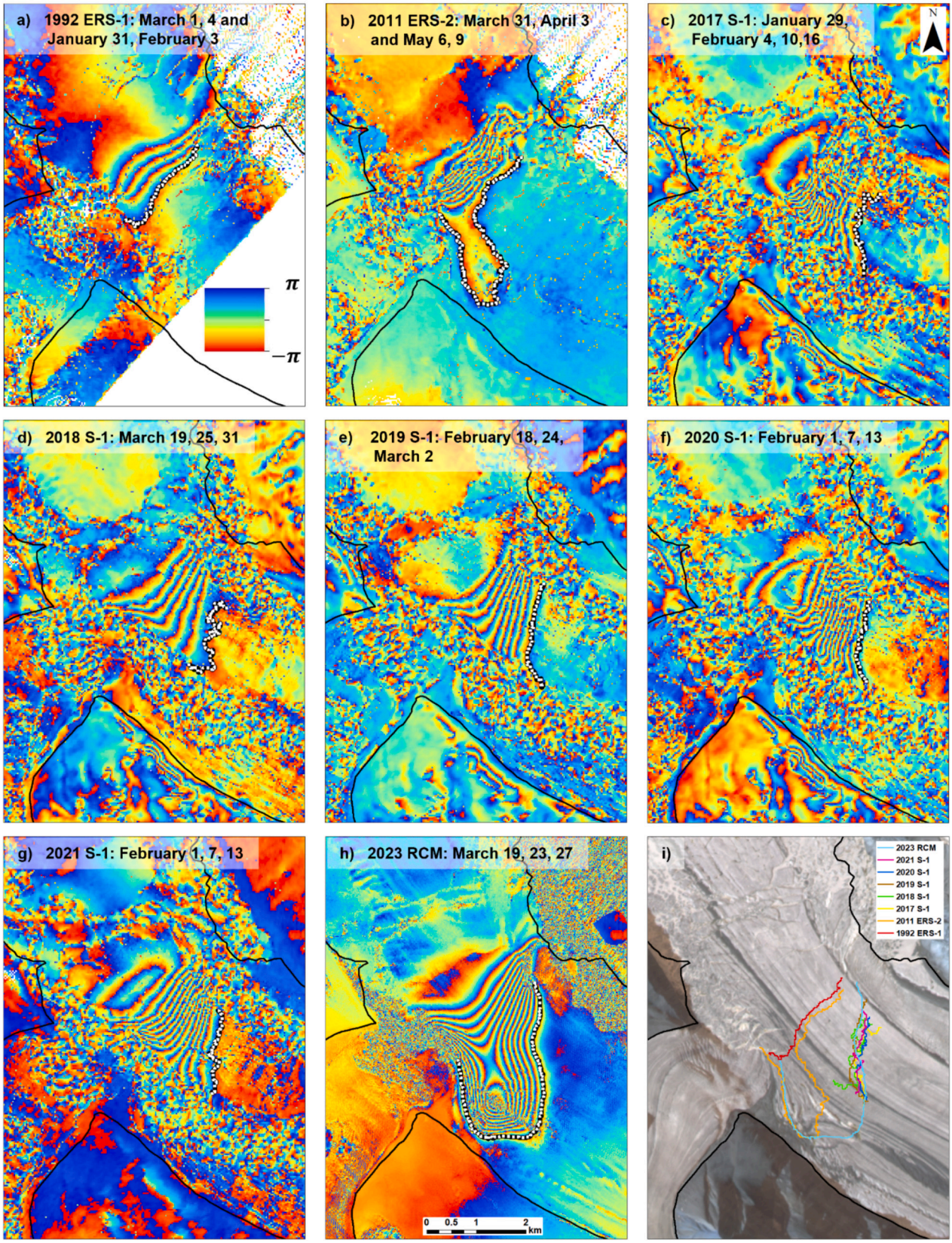

Fig. 5. Examples of double difference interferograms for each acquisition year from 1992 to 2023. (a-b) ERS 1/2, (c-g) Sentinel-1 (S1), and (h) RCM data and (i) delineated hinge-line positions overlaying a true-colour Planet image (Planet Team, 2017) acquired on 19 September 2023. The outline of Milne Glacier is shown with black lines.

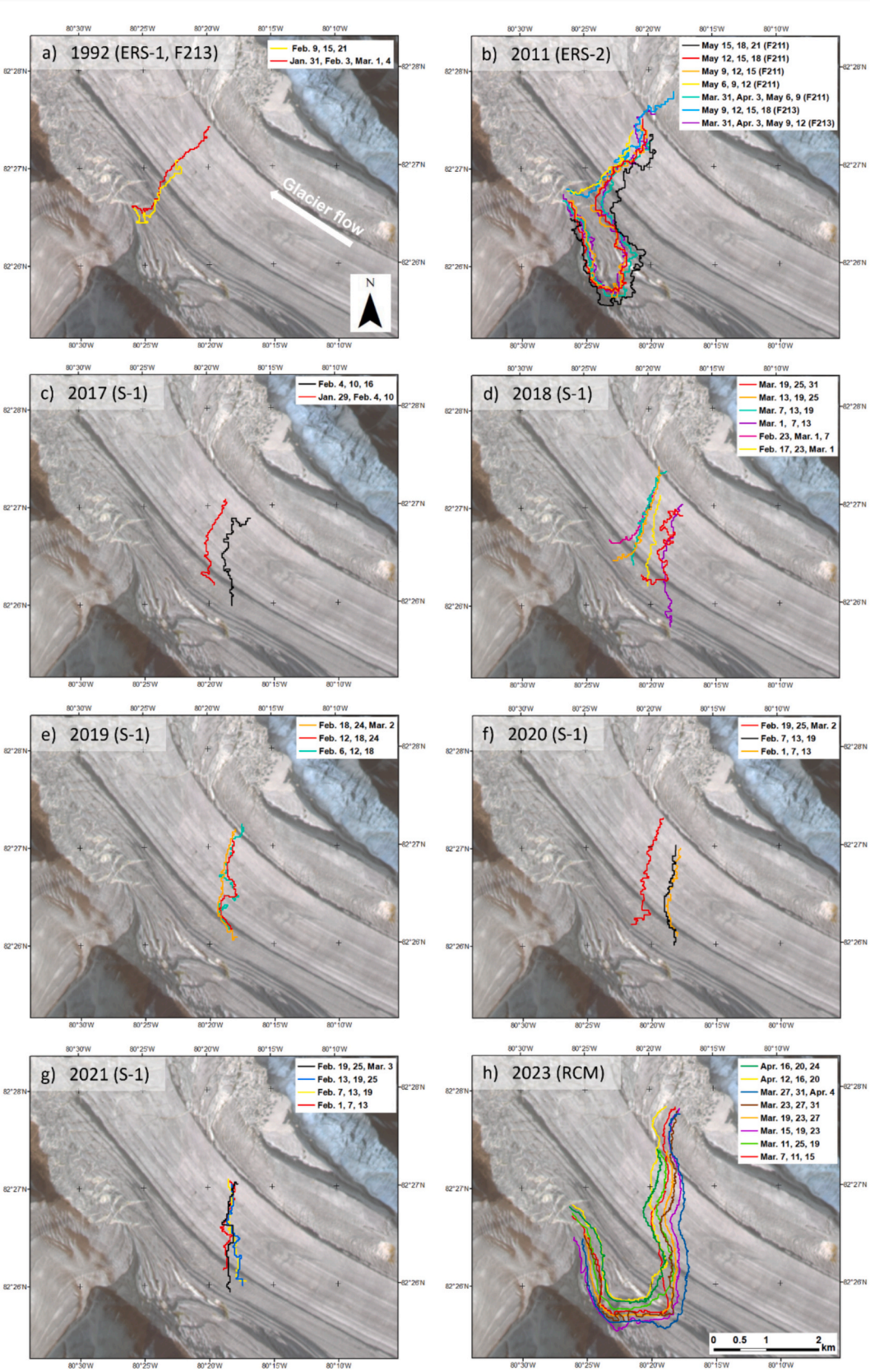

Fig. 6. DDInSAR-derived hinge-line locations of Milne Glacier between 1992 and 2023 overlying a true-colour Planet image (Planet Team, 2017) acquired on 19 July 2023.

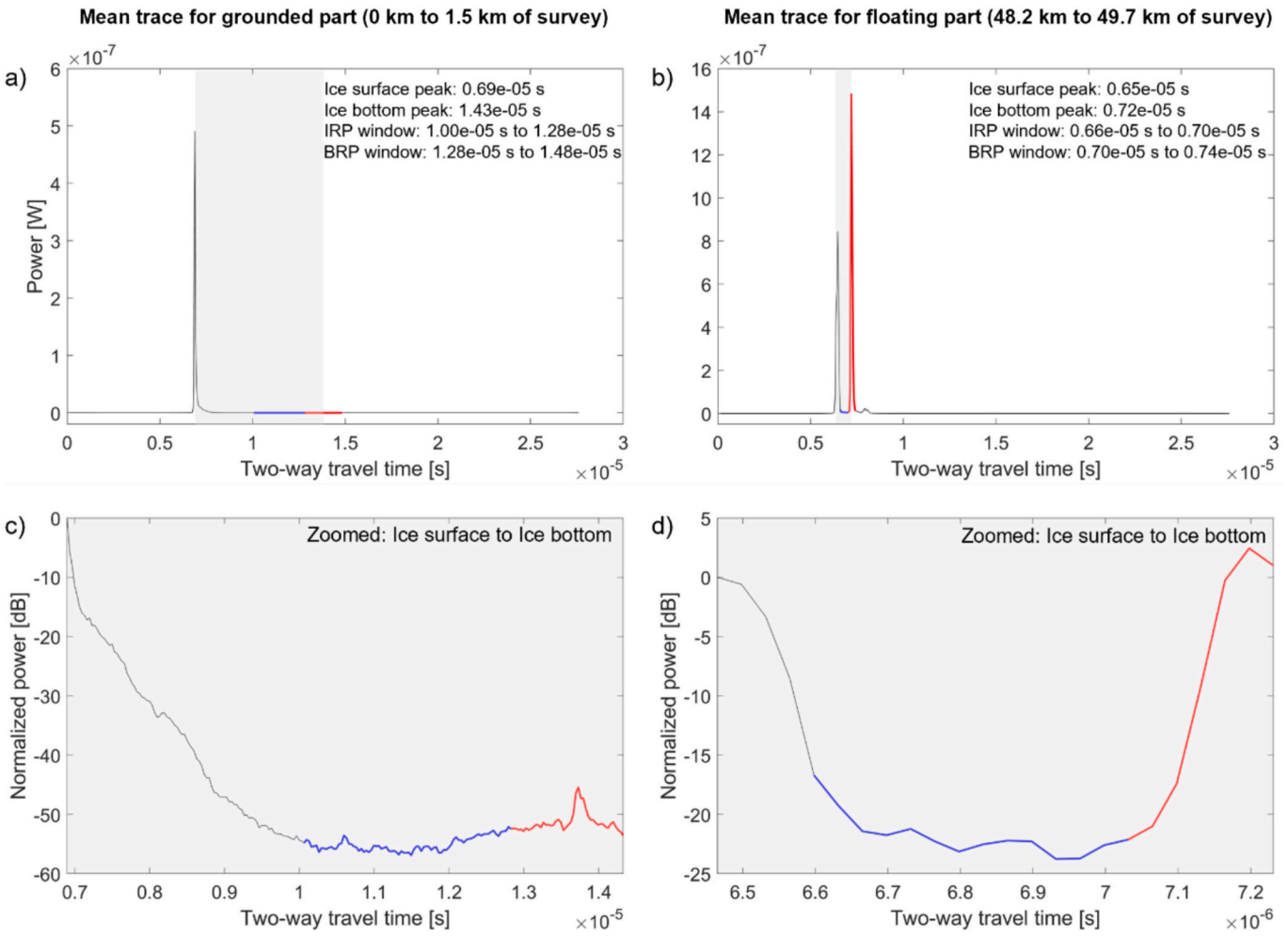

Fig. 7. IceBridge MCoRDS 3 radar survey of the Milne Glacier in 2014. (a) Mean signal trace for the first 100 observations (0 km to 1.5 km of the survey with thickness varying from 529 m to 714 m and a mean thickness of 628 m) corresponding to the accumulation zone of the Milne Glacier and (b) for the last 100 observations (48.2 km to 49.7 km of the survey with thickness varying from 58 m to 79 m and a mean thickness of 65 m) corresponding to the glacier tongue. Signal traces zoomed-in to the records between the ice surface peak and the ice bottom peak, a zone highlighted by grey shading colour, for (c) glacier accumulation zone and (d) glacier tongue. The surface signal attenuates much faster in the glacier tongue (b, d) than at the top of the glacier (a, c). IRP and BRP windows are marked by blue and red colours respectively. (For interpretation of the references to colour in this figure legend, the reader is referred to the web version of this article.)

the ice tongue in this location described by Schmeltz et al. (2001)."

Fig. 6 shows all the hinge-lines delineated for the years of SAR observations between 1992 and 2023. These hinge-line locations indicate that the most pronounced retreat of the Milne Glacier grounding line occurred in a large notch pointing up-glacier near the western margin of the glacier starting in 2011. The datasets acquired in 2011, 2017, 2018, 2020, and 2023 revealed pronounced variations in the HL_{LW} and HL_{SW} bounds, considering the low tidal range in the area. For instance, the maximum predicted range of tides for the period of SAR acquisitions in 2023 was 0.37 m and the distance between HL_{LW} – HL_{SW} bounds varied between ~400 and ~ 750 m along the notch in the western margin and between ~250 and ~ 450 m along the eastern margin of the glacier in 2023 (Fig. 6 h). This relatively large distance between the HL_{LW} – HL_{SW} bounds is consistent with the fact that the HL_{LW} – HL_{SW} bounds can be one to two orders of magnitude wider (Mohajerani et al., 2021; Chen et al., 2023) than the width calculated from hydrostatic equilibrium based on tide height, bed and surface slopes (Tsai and Gudmundsson, 2015). The difference in the span of HL_{LW} – HL_{SW} bounds across the glacier is in agreement with bed slope values derived from the BedMachine V005 dataset (Morlighem et al., 2020) and recent observations by Rignot et al. (2014) that these bounds have a larger span when covering shallow bed slopes. The span of the HL_{LW} – HL_{SW} bounds also depends on the type of bed (i.e., deformable vs. hard), seawater intrusions in the subglacial channels, and other ice-specific and/or environmental factors (Chen et al., 2023, Rignot et al., 2024).

4.2. *Grounding-line locations from airborne and ground-based radar data*

The proposed adaptive-window approach to determine the BRP and IRP integral limits was more suitable compared to the conventional symmetric or asymmetric fixed time window limits used by Gades et al. (2000) and Copland and Sharp (2001), because it accounted for the substantial differences in the radar signal patterns in the grounded and floating parts of the Milne Glacier. In particular, the IceBridge radar surface signal propagated much deeper into the ice layer located within the high-elevation Milne Glacier accumulation zone (Fig. 7). This zone is associated with thick, cold, and likely more homogeneous ice structure than within the Milne Glacier terminus zone associated with relatively thin, warm, and likely heterogeneous ice at lower elevations.

IceBridge radar signal analysis for grounding-line delineation along the central line of Milne Glacier (Fig. 8 c) was based on the BRP, NBRP and NIRP coefficients shown in Fig. 8 (a) and (b). Fig. 8 (a) shows a sharp increase in the BRP signal between km 40 and 50 of the airborne survey, which suggests a change in conditions at the base of the glacier. NBRP and NIRP coefficients were plotted together to assess the power returned from basal surface of the ice relative to power returned from within the

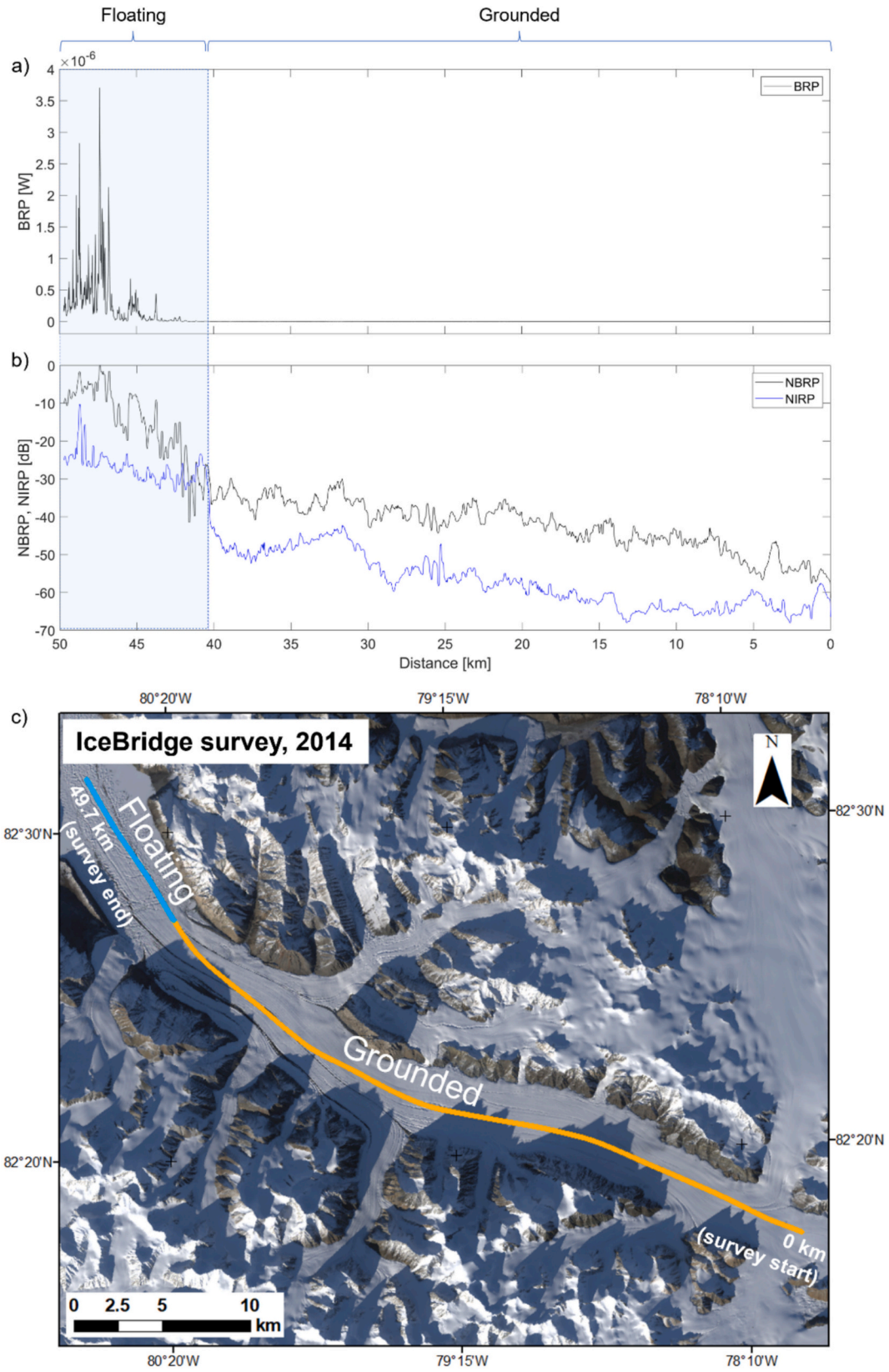

Fig. 8. IceBridge radar reflection power values plotted in the direction of Milne Glacier flow. (a) BRP calculated for the IceBridge radar signal; (b) Normalized BRP and IRP (NBRP and NIRP) coefficients, where NBRP values are consistently higher than NIRP values except for a short region between 40 and 42 km where there were crevasses/rifts. The dashed blue line corresponds to the region where BRP, NBRP and NIRP values start to increase due to the glacier transition from grounded to floating. (c) Airborne IceBridge radar survey over the Milne Glacier centerline acquired on 1 April 2014 overlaying a true-colour Landsat-8 optical image acquired on 13 September 2018. Based on the NBRP and NIPR analysis, the survey parts were highlighted by orange and blue colours that correspond to the grounded and floating parts of the glacier, respectively. (For interpretation of the references to colour in this figure legend, the reader is referred to the web version of this article.)

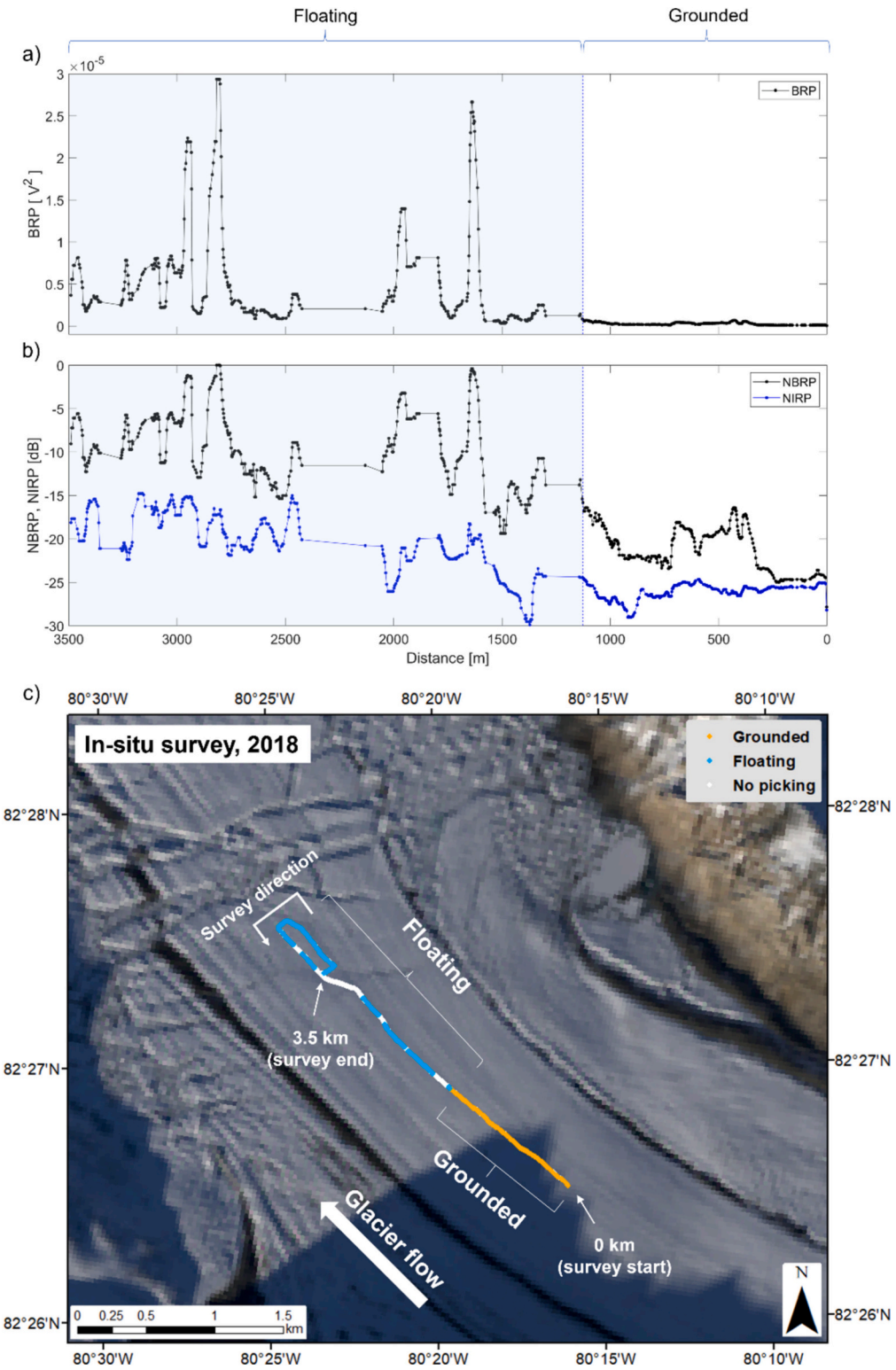

Fig. 9. Milne Glacier in-situ radar survey acquired on 13–14 July 2018. (a) BRP values. (b) NBRP and NIRP values. (c) Map of transect overlying a true-colour Landsat-8 optical image acquired on 13 September 2018.

ice column (Fig. 8 b). The NIRP coefficients were consistently lower than NBRP values except for several values between km 40 and ~ 42 of the survey, where crevasses and/or rifts were observed in the field and in SAR images. This suggests that there was no significant reduction in the amount of microwave energy that reached the glacier bed; hence, NBRP coefficients were reliable for the entire survey except for the crevassed region where NIRP values exceeded NBRP values. Normalized values also demonstrated a sharp increase in both NIRP and NBRP right after 40 km of the survey, and both coefficients were consistently higher within 40 to 50 km of the survey (highlighted in blue in Fig. 8) than before km 40 of the survey. We interpreted this as the transition between the grounded and floating portion of the glacier and picked the spot where relatively sharp increases in both NIRP and NBRP values were observed as the boundary between them.

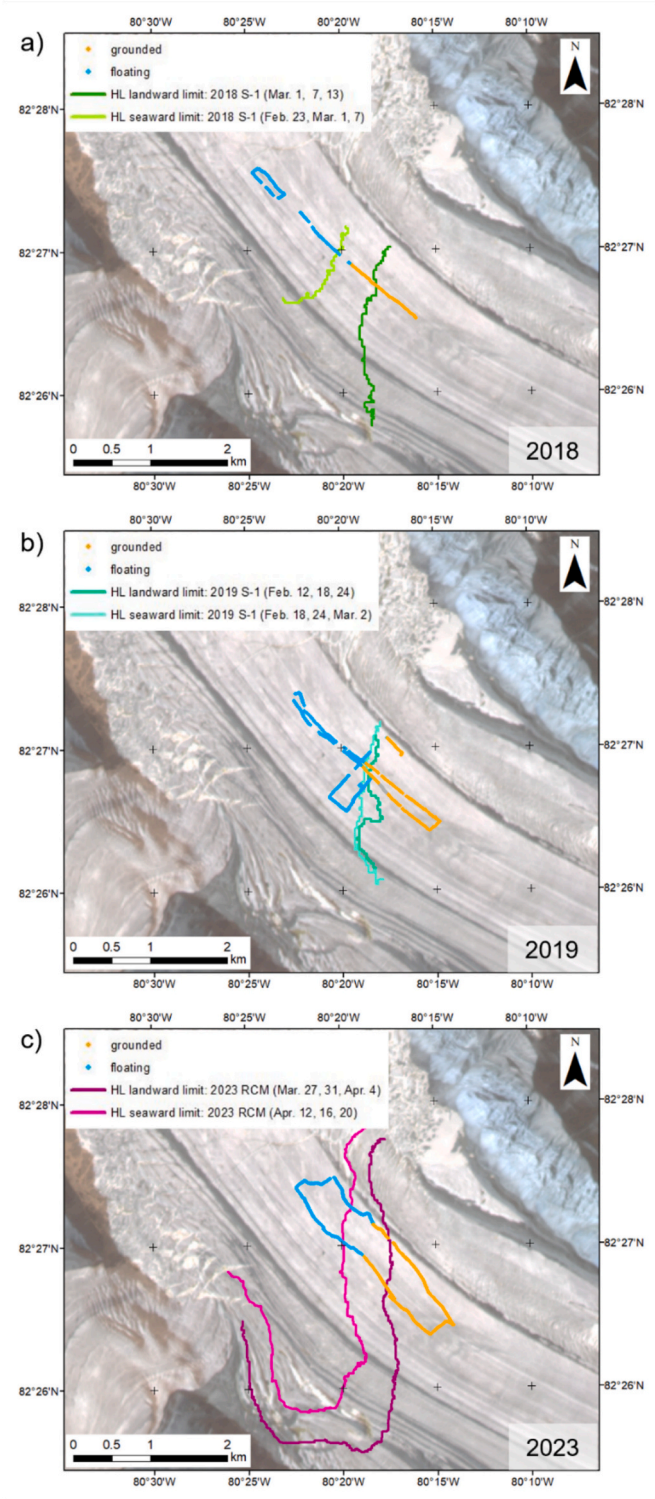

Fig. 10. The landward and seaward hinge-line bounds (HL_{LW} - HL_{SW}) of Milne Glacier derived from DDInSAR datasets for 2018 (a), 2019 (b), 2023 (c) and ground-based radar transects delineating floating (blue) and grounded (orange) parts of the glacier. (For interpretation of the references to colour in this figure legend, the reader is referred to the web version of this article.)

Ground-based in-situ IPR results were also analyzed based on BRP, NBRP, and NIRP values (panels a and b in Fig. 9, S4.1 and S4.2). Tracks of the in-situ surveys in 2018, 2019, and 2023 are presented in panels c of Fig. 9, S4.1 and S4.2. In some areas the presence of ice cracks caused scattering effects which compromised the bottom reflection of the IPR signal. As a consequence, the ice bottom was not picked in these locations (shown by white sections of the transect in Fig. 9 c).

NBRP coefficients in 2018 and 2019 were consistently higher than NIRP values suggesting that the bottom signal was not significantly affected by attenuation within the ice column. The 2023 dataset (Fig. S4.2 b) was characterized by higher NIRP values than in 2018 and 2019, which were likely caused by enhanced melt on Milne Glacier at the end of July in 2023. However, in general, NBRP values were still higher than NIRP values, suggesting that the bed signal was still captured in 2023. Similar to our 2014 radar results, the pronounced increase in BRP coincided with the increase in NIRP and/or NBRP and then both coefficients tended to be higher and more variable within the blue zones in Fig. 9 b, S4.1 b and S4.2 b where the glacier is afloat.

The abrupt rise in BRP, NBRP and NIRP coefficients, along with the shift towards increased variability, we noticed in our 2014–2023 radar datasets were interpreted as a change of the underlying medium, also associated with change of ice properties (e.g., ice temperature, liquid water content, and structure). Therefore, this shift in the coefficients was marked as the boundary between grounded (orange) and floating ice (blue) along the transect. Thus, we can conclude that both airborne and ground-based radar observations had lower and more consistent NBRP and NIRP values in the grounded part of the Milne Glacier relative to the floating ice tongue.

4.3. Comparative analysis of satellite SAR and in-situ IPR-based results. Milne glacier grounding-line retreat

Our comparison of satellite DDInSAR and ground-based IPR results is shown in Fig. 10. Floating (in blue) and grounded (in orange) parts of the glacier, delineated based on NBRP and NIRP values, were plotted along with HL_{LW} and HL_{SW} bounds of hinge-line migration retrieved from our DDInSAR results for the corresponding years. For all three years of observations, the IPR-derived glacier transition from the grounded to floating ice corresponded well with the DDInSAR-derived HL_{LW} - HL_{SW} bounds. For 2018, the IPR grounding line was observed 447 m down-glacier from HL_{LW} and 187 m upglacier of HL_{SW} bounds (Fig. 10 a). The 2019 SAR dataset likely missed much of the full variability in hinge-line positions due to only a few DDInSAR results available for our analysis; however, the IPR-derived grounding line was located close to the two available hinge lines (Fig. 10 b): 79 m and 147 m (measured along the eastern and western transects respectively) down-glacier of HL_{LW} and 6 m and 92 m (along the eastern and western transects) down-glacier of HL_{SW} bounds. The distances were measured along the stretched narrow loop (i.e., big loop in Fig. S4.1). The comparison of our 2023 IPR and DDInSAR results was based on well-characterized HL_{LW} – HL_{SW} bounds and two IPR lines (Fig. 10 c). We found that, similar to the 2018 results, the IPR-derived grounding line was withing the HL_{LW} - HL_{SW} bounds of the migration zone delineated from DDInSAR results: 269 m and 521 m (measured along the eastern and western transects respectively) down-glacier from HL_{LW} and 367 and 298 m (along the eastern and western transects) up-glacier of HL_{SW} bounds.

Our IPR and DDInSAR-derived datasets were used to quantify the Milne Glacier grounding-line retreat between 1966 and 2023. Based on the aerial and ground-based radar surveys of the Milne Glacier between 1966 and 2023, the grounding line retreated by 3.1 km along the centreline of the glacier delineated for the 1966 flight (Fig. 11). The uncertainties associated with this result can be attributed to the uncertainties of georeferencing (i.e., 8.5 m) and Topcon positional measurements (i.e., 0.5 m). However, the total actual uncertainty might be larger and cannot be quantified due to the unknown uncertainty associated with flight navigation in 1966.

The HL_{LW} - HL_{SW} DDInSAR-derived bounds were used to assess the retreat of the grounding line along the western, central, and eastern transects between 2011 and 2023 (Fig. 12). The grounding-line retreat, calculated from HL_{SW} bounds (Fig. 12 a) was: 2 km, 0.44 km, and 0.26

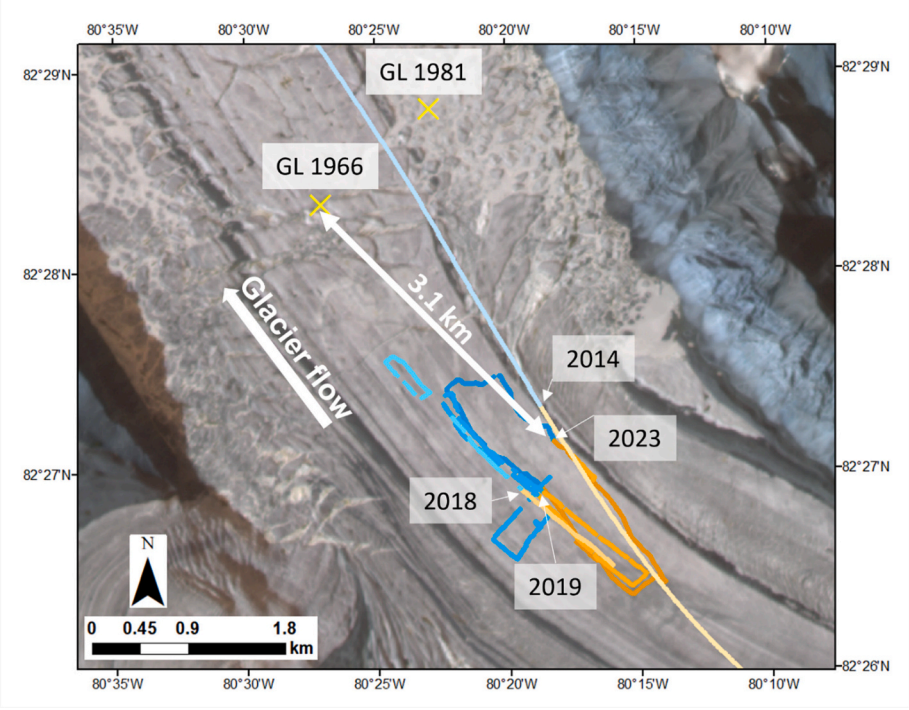

Fig. 11. Grounding-line (GL) retreat between 1966 and 2023 based on airborne and ground-based radar observations acquired over the central part and the ice flexure zone of Milne Glacier. Transects shown by different shades of orange and blue and concentrated around the glacier's flexure zone denote IPR observations acquired in 2014, 2018, 2019 and 2023. The location where the glacier transitions from grounded to floating is denoted by yellow crosses for 1966 and 1981 historical surveys, and by change in colours (orange – grounded part, blue – floating part) for the most recent IPR datasets. (For interpretation of the references to colour in this figure legend, the reader is referred to the web version of this article.)

km along the western, central, and eastern transects respectively. At the same time, the HL_{LW} retreat (Fig. 12 b) was 0.97 km, 0.83 m, and 0.44 km along the western, central, and eastern transects.

DDInSAR-derived annual average retreat rates of HL_{LW} and HL_{SW} bounds, and their means for the three periods of time (i.e., 2011–2023, 2011–2018, 2018–2023) are plotted along with the IPR-derived grounding-line annual average retreat rate between 1966 and 2023 in Fig. 13. Our results suggest that the grounding line in the eastern part of the glacier retreated at an average rate of 29 m yr^{-1}. However, the 2023 data show a similar to this retreat advance of the seaward hinge line further to the east, implying that the eastern section of the glacier was fairly stable between 2011 and 2023.

The central part of the glacier retreated at an average rate of 55 m yr^{-1} between 1966 and 2023 (based on IPR results), with the highest average retreat rate of 89 m yr^{-1} between 2011 and 2018 (based on DDInSAR HL_E results). Average retreat then slowed to 3 m yr^{-1} between 2018 and 2023. The slowdown of the average retreat rate during this period was caused by the advance of the seaward hinge line at an average rate of 14 m yr^{-1}, while the landward hinge line retreated at an average rate of 20 m yr^{-1}. The IceBridge thickness profile recorded in 2014 between the eastern and central transects suggest that the area between HL_{LW} – HL_{SW} bounds in 2023 (i.e., the zone around km 40 in Fig. S5.1) corresponds to the retrograde bed slope. Grounding-line retreat may be inhibited when the slope transitions to a prograde slope (km ~33–37 of the profile). Additional observations of bed geometry across the glacier are required, however, to better understand the processes driving grounding-line dynamics.

The western part of the glacier retreated at an average rate of 124 m yr^{-1} between 2011 and 2023. This part was also associated with the most pronounced retreat of the HL_{SW} bound due to the notch that has been expanding towards the central part of the glacier (i.e., hinge-line locations in 2011 vs. 2023 in Fig. 6 b and h). The overall grounding-line retreat derived from SAR datasets in recent decades was similar to the IPR-derived retreat along the glacier centreline. However, the enhanced retreat along the glacier's western margin highlights the importance of the full picture, provided by the SAR datasets in contrast to single IPR transects.

To summarize, the in-situ IPR-based grounding-line locations were in the HL_{LW} - HL_{SW} bounds derived from SAR observations. The combination of airborne, ground-based and SAR data allowed us to reveal the short-time positional variability of the grounding line and estimate its long-term retreat.

5. Discussion

Studies on grounding-line detection have moved from delineating the hinge or grounding line at a single time towards a complex and detailed understanding of the ice flexure zone spanning from hinge line to the landward limit of hydrostatic equilibrium (Friedl et al., 2020; Freer et al., 2023). The most recent studies that used multiple hinge-line locations over time to monitor the migration of the landward limit of the ice flexure zone over a short time scale, including a sub-daily (Rignot et al., 2024) scale, acknowledged that this region migrates depending on tides and glacier geometry, i.e., local surface and bed slopes (Chen et al., 2023; Freer et al., 2023; Milillo et al., 2022, and Mohajerani et al., 2021). In this study, we estimated the grounding-line average retreat rates based on the midpoint (HL_E) between the most landward and the most seaward hinge-line (HL_{LW} - HL_{SW}) locations that represent the landward limits of the ice flexure zone to address this issue.

We employed a DDInSAR analysis to explore the short-term variability in hinge-line locations. Our comparison of results from three different SAR systems demonstrated that continuous across-glacier monitoring of hinge-line locations, rather than point-based IPR observations, is important to reveal the spatial patterns of grounding-line retreat over a long period of time. Similarly to Chen et al. (2023), we found that a 6-day acquisition cycle was not frequent enough to provide

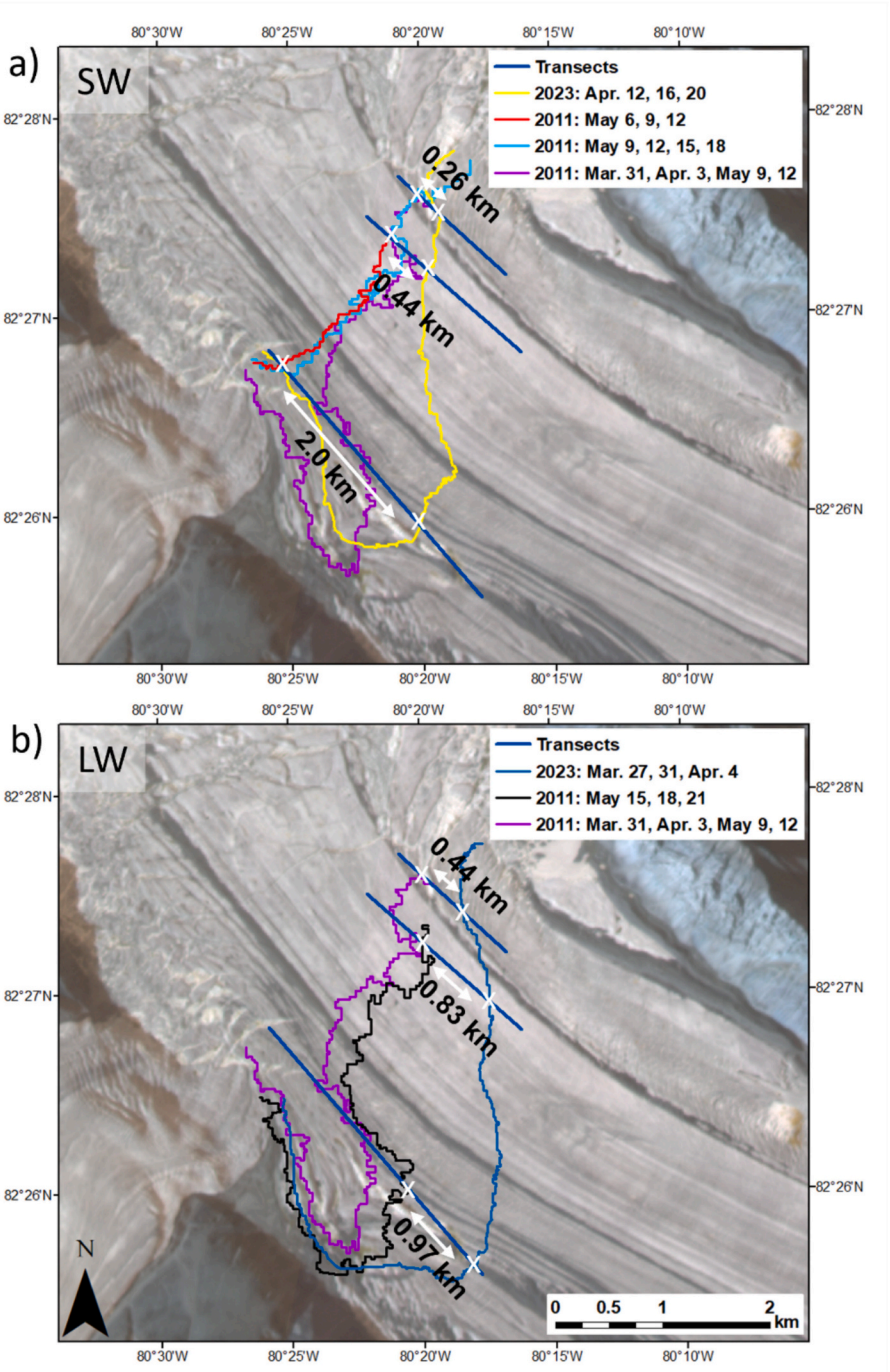

Fig. 12. Grounding-line retreat at the Milne Glacier based on the most seaward, HL_{SW}, (a) and the most landward, HL_{LW}, (b) hinge-line locations measured along the three transects (western, central, and eastern). Labelled distances demonstrate displacement between the most SW and LW positions of hinge-line observed between 2011 and 2023.

continuous across-glacier delineation of the Milne Glacier hinge line due to the loss of coherence. The image coherence ultimately depends on many factors such as viewing geometry, SAR platform characteristics, and changes in surface conditions. Other than melt, relatively high flow velocities is one of the main factors that affects image coherence (assuming the appropriate image geometry between the repeat acquisitions of a SAR platform) over glaciers. Milne Glacier has an average flow velocity of ~100 m yr^{-1}, which is typical for many glaciers in the Arctic (e.g., Van Wychen et al., 2020) and Antarctica (e.g., Mouginot et al., 2019). Thus, shorter acquisition time spans (i.e., 1 to 4 days) are useful to adequately delineate the hinge-line position across the entire glacier and show its positional variability (e.g., Milillo et al., 2022; Han and Lee, 2014). Our results derived from ERS-1/2 and RCM SAR imagery revealed a more pronounced retreat of the grounding line at the western edge than at the central and eastern parts of the glacier which would have been missed with 6 days DDInSAR results. A very high coherence between the repeat RCM acquisitions with high image resolution and suitable viewing geometry was achieved due to its frequent 4-day data acquisition capability. RCM provided the least noisy results at the finest spatial resolution of 10 m that allowed for a very detailed spatiotemporal hinge-line delineation of Milne Glacier. Thus, the use of RCM imagery enables an advanced and more precise quantification of

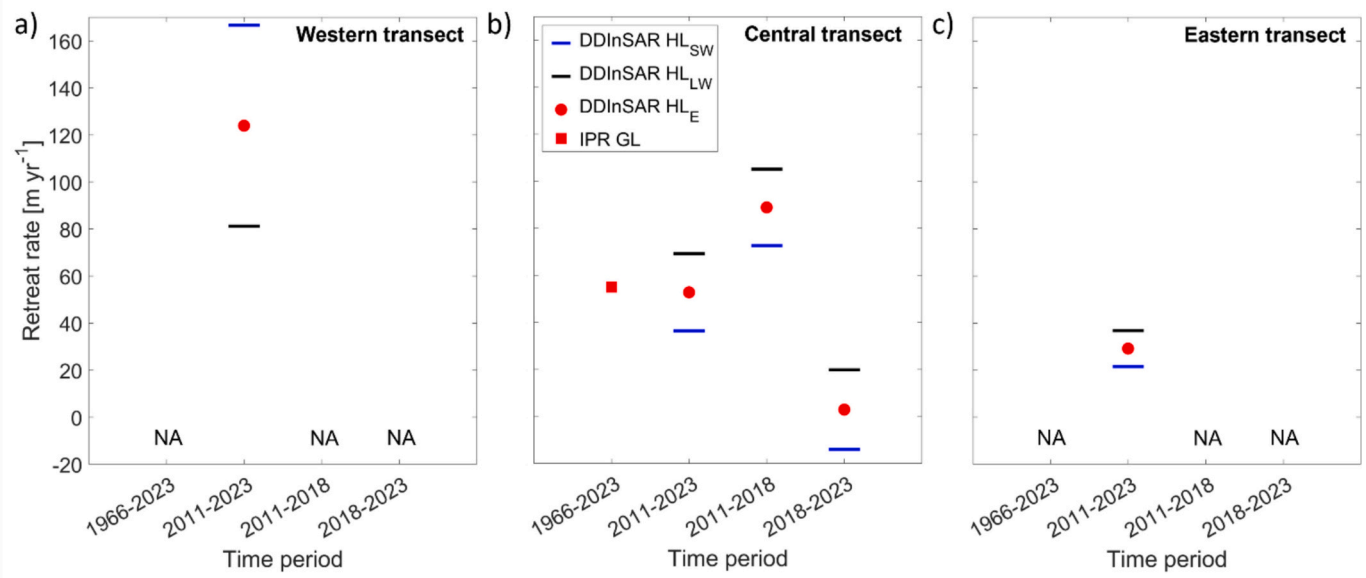

Fig. 13. Milne Glacier grounding-line average retreat rates per year for four different periods between 1966 and 2023 along three transects (Fig. 12) delineated over western, central, and eastern parts of the Milne Glacier based on DDInSAR-derived HL_{LW} and HL_{SW} bounds, their estimated means (HL_E), and IPR-derived grounding line (GL) locations.

grounding-line retreat as it can provide detailed information on its short-term variability that should be accounted for when the retreat is quantified over long time.

In this study, we also addressed a lack of direct and explicit comparison of DDInSAR-derived HL_{LW} - HL_{SW} bounds with grounding lines detected with the use of IPR techniques for datasets acquired between February and July of 2018, 2019, and 2023. A few recent studies compared a single hinge line derived with the use of DDInSAR to the

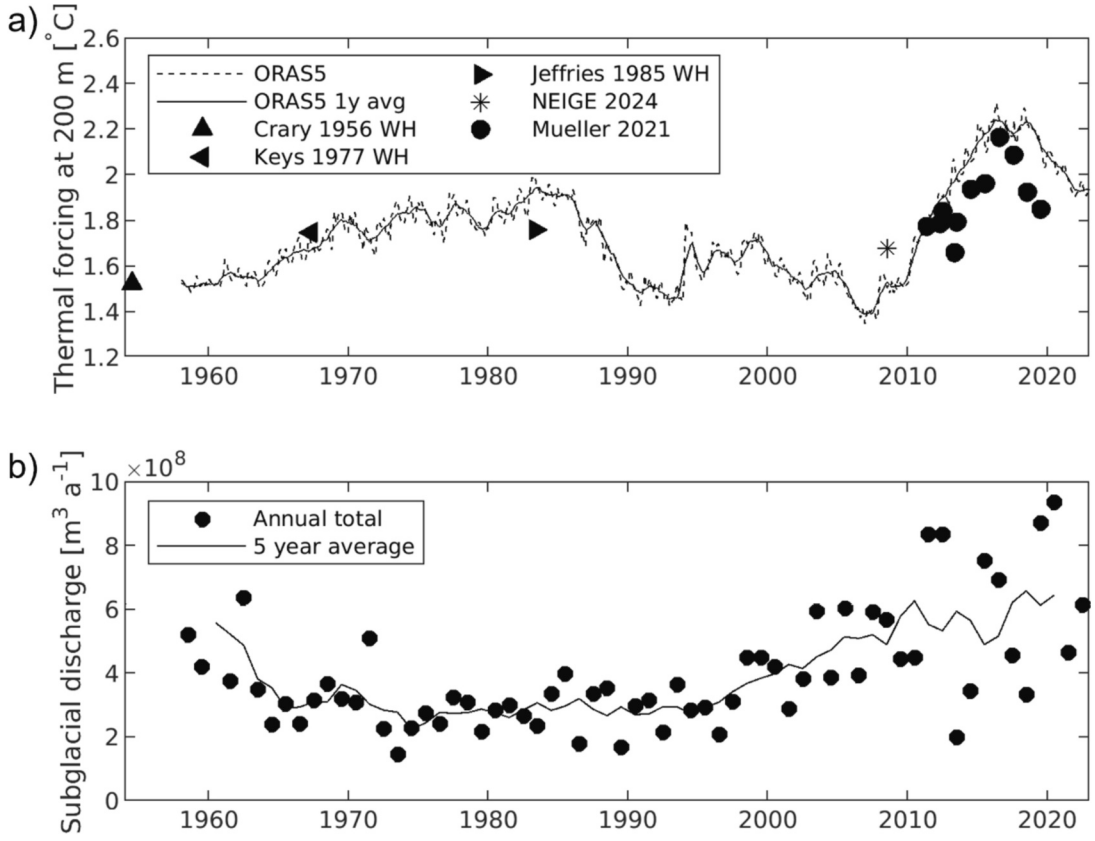

Fig. 14. Ocean thermal forcing and Milne Glacier subglacial discharge from 1955 to 2023. a) Ocean thermal forcing (i.e., temperature above the freezing point) at the 200 m depth offshore from Milne Fiord (grid point: 82.27 N, 91.61 W) according to ORAS5 reanalysis (Copernicus Climate Change Service and Climate Data, 2021). Observations shown with markers (NEIGE, 2024, Mueller et al., 2021, Jeffries, 1985, Keys, 1977, Crary, 1956,) are in a good agreement with ORAS5. b) Annual amount of subglacial discharge calculated by integrating the negative surface mass balance from RACMO2.3 (Noël et al., 2018) over Milne Glacier.

change in the power and/or brightness of IPR signal on radargrams (e.g., Bentley et al., 2023; Khazendar et al., 2016) to distinguish between grounded and floating parts of glacier. However, these studies did not account on the variability of hinge-line locations due to tides. We addressed this gap in the literature by comparing the most landward and seaward locations of the Milne Glacier hinge line (HL_{LW} - HL_{SW}) against our in-situ IPR-derived grounding lines for the concurrent years. Our findings demonstrated that IPR-derived grounding line locations were within the DDInSAR-derived HL_{LW} - HL_{SW} bounds.

To more objectively detect the grounding line based on IPR data rather than rely on the radargram brightness, this study employed the modified power-based radar signal analysis (Copland and Sharp, 2001; Gades et al., 2000). We introduced an adaptive automated approach that used the standard deviations calculated in a sliding time windows along the signal trace to calculate NBRP and NIRP coefficients. Although the delineation of the grounding line based on the radar bed reflectivity can be often ambiguous due to various reasons, such as basal melt, wet bed, basal crevassing, and many others (MacGregor et al., 2011), some studies used the bed reflectivity to characterize bed properties (e.g., Khazendar et al., 2016; Gades et al., 2000). Analysis of the signal attenuation throughout the ice thickness is crucial for reliable interpretation of bed reflectivity as the power of the return signal can be dominated by variations in englacial attenuation (Matsuoka, 2011). Our NBRP and NIRP-based analysis of in-situ radar data suggested that the radar transects could be classified into two zones: 1) relatively low and stable level of IRP and BRP values that corresponded to the grounded ice, and 2) relatively high and variable level of IRP and BRP values that corresponded to the floating ice. Although the NIRP and NBRP-based approach did not fully explain physical properties of the ice and bed, it could be efficiently used to qualitatively assess changes in the radar signal and define patterns in the reflectivity coefficients to distinguish between the grounded and floating parts of the glacier. This approach assumes that the survey is acquired over a sufficient length of both grounded and floating parts of a glacier to correctly distinguish the NBRP and NIRP patterns within these sections. In this study, the transition between grounded and floating ice was defined manually based on a relatively sharp increase in both NBRP and NIRP coefficients. Further analysis of radar datasets for other glaciers is required to define if a quantitative algorithm can be incorporated into this method to define this transitional zone automatically.

Finally, the combined IPR and DDInSAR results revealed the Milne Glacier grounding-line average retreat rates over several periods between 1966 and 2023. In the last 57 years, the average retreat rate of the grounding line along the centreline of the glacier was 55 m yr^{-1}. The most dramatic changes were observed on the western edge of the glacier between 2011 and 2023 with an average retreat rate of 124 m yr^{-1}. The calculated average retreat rates are in agreement with changes in the ocean temperatures around Milne Fiord (Fig. 14 a) and subglacial discharge (Fig. 14 b). For instance, the highest average retreat rate of the grounding line at the center of the Milne Glacier was observed between the 2011 and 2018, when both thermal forcing and the amount of subglacial discharge peaked. After 2018, the average retreat rate of the grounding line at the center followed the decrease in thermal forcing.

The demonstrated close association between the Milne Glacier grounding-line retreat and changes in both, ocean thermal forcing and subglacial discharge suggests that these two variables likely drive the grounding-line retreat. This is consistent with Greenland-wide studies reporting that these two variables have a direct impact on submarine melt and marine-terminating glacier retreat (e.g., Slater et al., 2020; Slater et al., 2019; Cowton et al., 2018). Comparison of grounding line retreat at Milne Glacier with findings for analogous glacier systems in northern Greenland such as Petermann, Ryder, Steensby, 79 N glaciers, where glacier tongues flow into ice shelves protected by fjords of the Arctic Ocean, reveals similarities of the retreat processes. Millan et al. (2023) demonstrated that grounding line retreat and ice shelf volume loss for these systems were intimately linked to basal melt and ocean temperature, matching our analysis.

The glacier basal melt estimates for the last two decades were also in good agreement with our findings and suggested that the most pronounced basal melt occurs at the grounding line. The glacier tongue melt rates in northern Greenland varied between 10 and 15 m yr^{-1} (reported by Wilson et al., 2017 for the period from 2011 to 2015) which is slightly above what was numerically estimated for the Milne Glacier tongue (8.2 m yr^{-1} reported by Bonneau et al., 2024a for the period from 2011 and 2019), but of similar magnitude. At the Milne Glacier grounding line, vertical thinning due to basal melting was estimated to vary from 15 m yr^{-1} at shallower areas to 26 m yr^{-1} in deeper area and up to 32 m yr^{-1} at subglacial discharge locations (Bonneau et al., 2024a). These rates are within the range of rates obtained near the grounding lines of Petermann (10 to 100 m yr^{-1}), Ryder (37 to 49 m yr^{-1}) and 79N (21 to 60 m yr^{-1}) glaciers (Ciracì et al., 2023; Millan et al., 2023, and Wilson et al., 2017). Similar to the Greenland's glaciers (Millan et al., 2023), these pronounced ice losses led to the Milne Glacier acceleration near its grounding line after 2016 (Van Wychen et al., 2020). This change in velocity was preceded by the most pronounced grounding line retreat rates observed between 2011 and 2018 in this study. Milne Glacier is lagging behind many marine-terminating glaciers in the CAA that have been slowing down and retreating in the recent decades. This might suggest their transitioning to land-terminating glaciers and decrease of their ice discharge (Millan et al., 2017; Van Wychen et al., 2016).

The heterogeneity in grounding line retreat across Milne Fiord, i.e. the formation of the notch on its western side, is also similar to the observations at Petermann Glacier (Hogg et al., 2016; Ciracì et al., 2023). This glacier has experienced enhanced grounding line retreat that resulted in two inland-pointing notches associated with thinner ice near them (Hogg et al., 2016). The asymmetric retreat pattern of Milne Glacier with an inland-pointing notch on its western edge could be attributed to the variation of ice thickness and/or bathymetry across the Milne Glacier. The BedMachine V005 dataset also suggests that the grounded part of Milne Glacier (i.e., above the most landward hinge line observed in 2023) is thinner in the fast-retreating western portion of the glacier associated with the notch in comparison to the central and eastern regions of the glacier. However, the Milne Fiord bed downglacier of the hinge line is deeper on its western than on eastern side. This might suggest that deep and warm oceanic water could contribute to the grounding line retreat in the past decades. Modeling of the subglacial hydrology in Petermann suggests that the areas of enhanced grounding line retreat coincide with subglacial channel outlets and deeper bathymetry (Ciracì et al., 2023; Gadi et al., 2023). This is consistent with the Milne Fiord bathymetry and provides a possible explanation for the formation of the notch in the western margin of the grounding line.

6. Conclusions

In this study, we delineated multiple locations of the Milne Glacier hinge line for the years of 1992, 2011, and 2017–2021, and 2023 using spaceborne observations and compared them against airborne and ground-based radar datasets from 1966, 1981, 2014, 2018, 2019, and 2023. Based on these complementary datasets we quantified the grounding-line retreat between 1966 and 2023. We found that the glacier grounding line retreated by 3.1 km along the central line in the last 57 years and the average rate of retreat along the central line varied from 3 m yr^{-1} (2018–2023) to 89 m yr^{-1} (2011–2018), which was lower than the average rate of retreat of 124 m yr^{-1} (2011−2023) observed on the western edge of the glacier. Additional in-situ observations of ice thickness and bathymetry in the glacier flexure zone are required to better understand processes driving the glacier deterioration on its western edge. Our analysis of grounding-line retreat over the last half century will serve as a baseline for the future studies of cryosphere change as the Arctic becomes warmer.

In this study, we demonstrated that IPR-derived results were in the

HL_{LW} - HL_{SW} bounds that were taken to represent end members of hinge-line migration due to tides. This analysis addressed the lack of explicit comparison of in-situ IPR observations against DDInSAR-derived bounds of hinge line migration. Furthermore, our RCM DDInSAR analysis demonstrated pronounced hinge-line migration within the HL_{LW} - HL_{SW} zone on a short time scale. Continuous monitoring of the short-term migration of the hinge line will provide opportunities to better understand glacier-specific and environmental factors other than tides that affect this migration. In turn, the comprehensive understanding of the short-term positional variability of the hinge/grounding line will improve our understanding of long-term processes occurring in this important zone which is responsible for glacier dynamics and viability. Consistent RCM SAR coherent change detection coverage with 4 days time span over the Arctic, Greenland, and Antarctica glaciers could provide great opportunities for frequent and reliable hinge-line observations for glaciological research in the changing environment.

Funding

This project was supported by the: Natural Sciences and Engineering Research Council of Canada (YA: USRA 2018, CGS M 2019, and PGSD3–546559-2020; DM: RGPIN-2016-06244, RGPNS-2022-04875), W. Garfield Weston Foundation (YA: 2019–2020 Northern Research and Extended Stay Awards), Canada Foundation for Innovation (DM: 31410), Ontario Research Foundation (DM: 31410), Polar Continental Shelf Program (DM: 627–18; 651–19, 655–23), ArcticNet GO-Ice (YA, DM, and JB), Polar Knowledge Canada (YA and JB: NSTP 2018, 2019, and 2023), and the Leverhulme Trust Early Career Fellowship (AC: 2021–440).

CRediT authorship contribution statement

Yulia K. Antropova: Writing – review & editing, Writing – original draft, Software, Methodology, Investigation, Funding acquisition, Formal analysis, Conceptualization. **Derek Mueller:** Writing – review & editing, Supervision, Funding acquisition, Conceptualization. **Sergey V. Samsonov:** Writing – review & editing, Software, Formal analysis. **Alexander S. Komarov:** Writing – review & editing, Methodology, Investigation. **Jérémie Bonneau:** Writing – review & editing, Investigation. **Anna J. Crawford:** Writing – review & editing, Investigation.

Declaration of competing interest

None.

Data availability

The authors do not have permission to share RCM data, other satellite and airborne radar data are freely available; field data can be shared by request.

Acknowledgments

We are grateful to the Polar Continental Shelf Program for the logistical support that greatly facilitated all field work activities related to this study, and to the Research Computing Services at Carleton University for IT support. We thank all members of the 2018, 2019, and 2023 field campaigns in Milne Fiord, David T. Sandwell for advising on GMTSAR processing, and Brice Noël for providing RACMO2.3 data.

We acknowledge the use of RCM, ERS-1/2, Sentinel-1 data.

Some data used in this study were acquired by NASA's Operation IceBridge.We acknowledge the use of data products from CReSIS generated with support from the University of Kansas, NSF grant ANT-0424589, and NASA Operation IceBridge grant NNX16AH54G.

Appendix A. Supplementary data

Supplementary data to this article can be found online at https://doi.org/10.1016/j.rse.2024.114478.

References

Barber, D.G., McCullough, G., Babb, D., Komarov, A.S., Candlish, L.M., Lukovich, J.V., Asplin, M., Prinsenberg, S., Dmitrenko, I., Rysgaard, S., 2014. Climate change and ice hazards in the Beaufort Sea. Elem. Sci. Anth. 2, 000025. https://doi.org/10.12952/journal.elementa.000025.

Benn, D.I., Warren, C.R., Mottram, R.H., 2007. Calving processes and the dynamics of calving glaciers. Earth Sci. Rev. 82 (3–4), 143–179. https://doi.org/10.1016/j.earscirev.2007.02.002.

Bentley, M.J., Smith, J.A., Jamieson, S.S.R., Lindeman, M.R., Rea, B.R., Humbert, A., Lane, T.P., Darvill, C.M., Lloyd, J.M., Straneo, F., Helm, V., Roberts, D.H., 2023. Direct measurement of warm Atlantic intermediate water close to the grounding line of Nioghalvfjerdsfjorden (79° N) glacier, Northeast Greenland. Cryosphere 17 (5), 1821–1837. https://doi.org/10.5194/tc-17-1821-2023.

Bindschadler, R., Choi, H., Wichlacz, A., Bingham, R., Bohlander, J., Brunt, K., Young, N., 2011a. Getting around Antarctica: new high-resolution mappings of the grounded and freely-floating boundaries of the Antarctic ice sheet created for the international polar year. Cryosphere 5 (3), 569–588. https://doi.org/10.5194/tc-5-569-2011.

Bindschadler, R., Choi, H., Wichlacz, A., Bingham, R., Bohlander, J., Brunt, K., Young, N., 2011b. Getting around Antarctica: new high-resolution mappings of the grounded and freely-floating boundaries of the Antarctic ice sheet created for the international polar year. Cryosphere 5 (3), 569–588. https://doi.org/10.5194/tc-5-569-2011.

Bogorodsky, V.V., Bentley, C.R., Gudmandsen, P.E., Chebotareva, V., 1985. Radioglaciology, 1st ed 1. Springer, Netherlands. https://doi.org/10.1007/978-94-009-5275-1.

Bonneau, J., Laval, B. E.B.E., Mueller, D., Hamilton, A. K.A.K., Friedrichs, A. M.A.M., Forrest, A. L.A.L., 2021. Winter Dynamics in an Epishelf Lake: Quantitative Mixing Estimates and Ice Shelf basal channel ConsiderationsWinter dynamics in an Epishelf Lake: quantitative mixing estimates and ice shelf basal channel considerations. Journal of Geophysical Research: OceansJ. Geophys. Res. Oceans 126 (9), e2021JC017324. https://doi.org/10.1029/2021JC017324.

Bonneau, J., Laval, B.E., Mueller, D., Hamilton, A.K., Antropova, Y.K., 2024a. Heat Fluxes in a Glacial Fjord: The Role of Buoyancy-Driven Circulation and Offshore Forcing. Geophys. Res. Lett. https://doi.org/10.1029/2024GL111242.

Bonneau, J., Laval, B.E., Mueller, D., Hamilton, A.K., Forrest, A.L., 2024b. Unsteady circulation in a Glacial Fjord: a multiyear modeling study of Milne fiord. J. Geophys. Res. Oceans 129 (6), e2023JC020140. https://doi.org/10.1029/2023JC020140.

Chen, H., Rignot, E., Scheuchl, B., Ehrenfeucht, S., 2023. Grounding zone of Amery ice shelf, Antarctica, from differential synthetic-aperture radar interferometry. Geophys. Res. Lett. 50 (6), e2022GL102430. https://doi.org/10.1029/2022GL102430.

Ciracì, E., Rignot, E., Scheuchl, B., Tolpekin, V., Wollersheim, M., An, L., Milillo, P., Bueso-Bello, J.-L., Rizzoli, P., Dini, L., 2023. Melt rates in the kilometer-size grounding zone of Petermann glacier, Greenland, before and during a retreat. Proc. Natl. Acad. Sci. 120 (20), e2220924120. https://doi.org/10.1073/pnas.2220924120.

Copernicus Climate Change Service, Climate Data Store. (2021): ORAS5 global ocean reanalysis monthly data from 1958 to present. Copernicus Climate Change Service (C3S) Climate Data Store (CDS). DOI: 10.24381/cds.67e8eeb7.

Copernicus, 2022. Copernicus DEM– global and European digital ElevationModel (COP-DEM), GLO-30, ESA. Copernicus [dataset]. https://doi.org/10.5270/ESA-c5d3d65.

Copland, L., Sharp, M., 2001. Mapping thermal and hydrological conditions beneath a polythermal glacier with radio-echo sounding. J. Glaciol. 47 (157), 232–242. https://doi.org/10.3189/172756501781832377.

Cowton, T.R., Sole, A.J., Nienow, P.W., Slater, D.A., Christoffersen, P., 2018. Linear response of East Greenland's tidewater glaciers to ocean/atmosphere warming. Proc. Natl. Acad. Sci. 115 (31), 7907–7912. https://doi.org/10.1073/pnas.1801769115.

Crary, A.P., 1956. Geophysical studies along northern Ellesmere Island. Arctic, 154-165. CReSIS. 2021. In: 2014 Greenland P3 Data, Lawrence, Kansas. Digital Media, USA. http://data.cresis.ku.edu/.

CReSIS, 2016. CReSIS Radar Depth Sounder Data, Lawrence, Kansas. Digital Media, USA. http://data.cresis.ku.edu/.

Dowdeswell, Julian, Jeffries, Martin, 2017. Arctic Ice Shelves: An Introduction. https://doi.org/10.1007/978-94-024-1101-0_1.

Freer, B.I.D., Marsh, O.J., Hogg, A.E., Fricker, H.A., Padman, L., 2023. Modes of Antarctic tidal grounding line migration revealed by ice, cloud, and land elevation Satellite-2 (ICESat-2) laser altimetry. Cryosphere 17 (9), 4079–4101. https://doi.org/10.5194/tc-17-4079-2023.

Fricker, H.A., Coleman, R., Padman, L., Scambos, T.A., Bohlander, J., Brunt, K.M., 2009. Mapping the grounding zone of the Amery ice shelf, East Antarctica using InSAR, MODIS and ICESat. Antarctic Sci. 21 (5), 515–532. https://doi.org/10.1017/S095410200999023X.

Friedl, P., Weiser, F., Fluhrer, A., Braun, M.H., 2020. Remote sensing of glacier and ice sheet grounding lines: a review. Earth Sci. Rev. 201, 102948. https://doi.org/10.1016/j.earscirev.2019.102948.

Gades, A.M., Raymond, C.F., Conway, H., Jagobel, R.W., 2000. Bed properties of Siple dome and adjacent ice streams, West Antarctica, inferred from radio-echo sounding measurements. J. Glaciol. 46 (152), 88–94. https://doi.org/10.3189/172756500781833467.

Gadi, R., Rignot, E., Menemenlis, D., 2023. Modeling ice melt rates from seawater intrusions in the grounding zone of Petermann Gletscher, Greenland. Geophys. Res. Lett. 50 (24), e2023GL105869. https://doi.org/10.1029/2023GL105869.
Gardner, A.S., Moholdt, G., Wouters, B., Wolken, G.J., Burgess, D.O., Sharp, M.J., Cogley, J.G., Braun, C., Labine, C., 2011. Sharply increased mass loss from glaciers and ice caps in the Canadian Arctic archipelago. Nature 473 (7347), 357–360. https://doi.org/10.1038/nature10089.
Hamilton, A.K., 2016. Ice-Ocean Interactions in Milne Fiord. PhD thesis,. University of British Columbia.
Han, H., Lee, H., 2014. Tide deflection of Campbell glacier tongue, Antarctica, analyzed by double-differential SAR interferometry and finite element method. Remote Sens. Environ. 141, 201–213. https://doi.org/10.1016/j.rse.2013.11.002.
Hattersley-Smith, G., 1969. Recent observations on the surging Otto glacier, Ellesmere Island. Can. J. Earth Sci. 6 (4), 883–889. https://doi.org/10.1139/e69-090.
Hogg, A.E., Shepherd, A., Gourmelen, N., Engdahl, M., 2016. Grounding line migration from 1992 to 2011 on Petermann glacier, North-West Greenland. J. Glaciol. 62 (236), 1104–1114. https://doi.org/10.1017/jog.2016.83.
Horgan, H.J., Anandakrishnan, S., 2006. Static grounding lines and dynamic ice streams: evidence from the Siple coast, West Antarctica. Geophys. Res. Lett. 33 (18). https://doi.org/10.1029/2006GL027091.
Intergovernmental Panel on Climate Change (IPCC), 2019. Special Report on the Ocean and Cryosphere in a Changing Climate. Retrieved from. https://www.ipcc.ch/srocc/home.
Jeffries, M.O., 1984. Milne glacier, northern Ellesmere Island, N.W.T., Canada: a surging glacier? J. Glaciol. 30 (105), 251–253.
Jeffries, M.O., 1985. Physical, Chemical and Isotopic Investigations of Ward Hunt Ice Shelf and Milne Ice Shelf, Ellesmere Island, NWT. PhD thesis.. University of Calgary.
Jeffries, M.O., 1986. Glaciers and the morphology and structure of Milne ice shelf, Ellesmere Island, N.W.T., Canada. Arct. Alp. Res. 18 (4), 397–405. https://doi.org/10.2307/1551089.
Keys, J.E., 1977. Water Regimes of Ice-Covered Fiords and Lakes. PhD thesis.. McGill University.
Khazendar, A., Rignot, E., Schroeder, D.M., Seroussi, H., Schodlok, M.P., Scheuchl, B., Mouginot, J., Sutterley, T.C., Velicogna, I., 2016. Rapid submarine ice melting in the grounding zones of ice shelves in West Antarctica. Nat. Commun. 7 (1), 13243. https://doi.org/10.1038/ncomms13243.
Le Meur, E., Sacchettini, M., Garambois, S., Berthier, E., Drouet, A.S., Durand, G., Young, D., Greenbaum, J.S., Holt, J.W., Blankenship, D.D., Rignot, E., Mouginot, J., Gim, Y., Kirchner, D., de Fleurian, B., Gagliardini, O., Gillet-Chaulet, F., 2014. Two independent methods for mapping the grounding line of an outlet glacier – an example from the astrolabe glacier, Terre Adélie, Antarctica. Cryosphere 8 (4), 1331–1346. https://doi.org/10.5194/tc-8-1331-2014.
Lenaerts, J.T.M., van Angelen, J.H., van den Broeke, M.R., Gardner, A.S., Wouters, B., van Meijgaard, E., 2013. Irreversible mass loss of Canadian Arctic archipelago glaciers. Geophys. Res. Lett. 40 (5), 870–874. https://doi.org/10.1002/grl.50214.
MacGregor, J.A., Anandakrishnan, S., Catania, G.A., Winebrenner, D.P., 2011. The grounding zone of the Ross ice shelf, West Antarctica, from ice-penetrating radar. J. Glaciol. 57 (205), 917–928. https://doi.org/10.3189/002214311798043780.
Matsuoka, K., 2011. Pitfalls in radar diagnosis of ice-sheet bed conditions: lessons from englacial attenuation models. Geophys. Res. Lett. 38 (5). https://doi.org/10.1029/2010GL046205.
Milillo, P., Rignot, E., Rizzoli, P., Scheuchl, B., Mouginot, J., Bueso-Bello, J.L., Prats-Iraola, P., Dini, L., 2022. Rapid glacier retreat rates observed in West Antarctica. Nat. Geosci. 15 (1), 1. https://doi.org/10.1038/s41561-021-00877-z.
Millan, R., Mouginot, J., Rignot, E., 2017. Mass budget of the glaciers and ice caps of the queen Elizabeth Islands, Canada, from 1991 to 2015. Environ. Res. Lett. 12 (2), 024016. https://doi.org/10.1088/1748-9326/aa5b04.
Millan, R., Mouginot, J., Derkacheva, A., Rignot, E., Milillo, P., Ciraci, E., Dini, L., Bjørk, A., 2022. Ongoing grounding line retreat and fracturing initiated at the Petermann glacier ice shelf, Greenland, after 2016. Cryosphere 16 (7), 3021–3031. https://doi.org/10.5194/tc-16-3021-2022.
Millan, R., Jager, E., Mouginot, J., Wood, M.H., Larsen, S.H., Mathiot, P., Jourdain, N.C., Bjørk, A., 2023. Rapid disintegration and weakening of ice shelves in North Greenland. Nat. Commun. 14 (1), 6914. https://doi.org/10.1038/s41467-023-42198-2.
Mingo, L., Flowers, G.E., 2010. Instruments and methods: An integrated lightweight ice-penetrating radar system. J. Glaciol. 56 (198), 709–714.
Mohajerani, Y., Jeong, S., Scheuchl, B., Velicogna, I., Rignot, E., Milillo, P., 2021. Automatic delineation of glacier grounding lines in differential interferometric synthetic-aperture radar data using deep learning. Sci. Rep. 11 (1), 1. https://doi.org/10.1038/s41598-021-84309-3.
Morlighem, M., et al., 2020. IceBridge BedMachine Greenland, Version 5. NASA National Snow and Ice Data Center Distributed Active Archive Center, Boulder, Colorado USA. https://doi.org/10.5067/VLJ5YXKCNGXO.
Mortimer, C.A., Copland, L., Mueller, D.R., 2012. Volume and area changes of the Milne Ice Shelf, Ellesmere Island, Nunavut, Canada, since 1950. J. Geophys. Res. Earth Surface; Washington 117 (4). https://doi.org/10.1029/2011JF002074.
Mouginot, J., Rignot, E., Scheuchl, B., 2019. Continent-wide, interferometric SAR phase, mapping of Antarctic ice velocity. Geophys. Res. Lett. 46 (16), 9710–9718. https://doi.org/10.1029/2019GL083826.
Mueller, D., Copland, L., Jeffries, M.O., 2017. Changes in Canadian Arctic ice shelf extent since 1906. In: Arctic Ice Shelves and Ice Islands, pp. 109–148.
Mueller, D., Hamilton, A.K., Bonneau, J., Friedrichs, D.M., Rajewicz, J.S., White, A., et al., 2021. Milne Fiord CTD (Conductivity, Temperature, Depth) Profiles, 2008-2019 [dataset]. https://doi.org/10.21963/12102.
Narod, B.B., Clarke, G.K.C., Prager, B.T., 1988. Airborne UHF radar sounding of glaciers and ice shelves, northern Ellesmere Island, Arctic Canada. Can. J. Earth Sci. 25 (1), 95–105. https://doi.org/10.1139/e88-010.
NEIGE, 2024. Profils physico-chimiques de la colonne d'eau de lacs et de fjords de la côte nord de l'île d'Ellesmere, v. 1.2.0 (1954–2022). Nordicana D27. https://doi.org/10.5885/45445CE-7B8194DB81754841.
Noël, B., van de Berg, W.J., Lhermitte, S., Wouters, B., Schaffer, N., van den Broeke, M. R., 2018. Six decades of glacial mass loss in the Canadian Arctic archipelago. J. Geophys. Res. Earth 123 (6), 1430–1449. https://doi.org/10.1029/2017JF004304.
Paden, J., Li, J., Leuschen, C., Rodriguez-Morales, F., Hale, R., 2010. Updated 2019. IceBridge MCoRDS L2 Ice Thickness, Version 1. [IRMCR2_20140401_03]. NASA National Snow and Ice Data Center Distributed Active Archive Center, Boulder, Colorado USA. https://doi.org/10.5067/GDQ0CUCVTE2Q.
Pawlowicz, R., Beardsley, B., Lentz, S., 2002. Classical tidal harmonic analysis including error estimates in MATLAB using T_TIDE. Comput. Geosci. 28 (8), 929–937. https://doi.org/10.1016/S0098-3004(02)00013-4.
Planet Team, 2017. Planet Application Program Interface. In Space for Life on Earth, San Francisco, CA. https://api.planet.com.
Porter, C., Morin, P., Howat, I., Noh, M.J., Bates, B., Peterman, K., Keesey, S., Schlenk, M., Gardiner, J., Tomko, K., Willis, M., Kelleher, C., Cloutier, M., Husby, E., Foga, S., Nakamura, H., Platson, M., Wethington Jr., M., Williamson, C., Bauer, G., Enos, J., Arnold, G., Kramer, W., Becker, P., Doshi, A., D'Souza, C., Cummens, P., Laurier, F., Bojesen, M., 2023. ArcticDEM. Harvard Dataverse V1. https://doi.org/10.7910/DVN/OHHUKH.
Prager, B.T., 1983. Digital Signal Processing of UHF Radio Echo Sounding Data from northern Ellesmere Island. University of British Columbia. https://doi.org/10.14288/1.0052939.
RGI 7.0 Consortium, 2023. Randolph Glacier Inventory - A Dataset of Global Glacier Outlines, Version 7.0. NSIDC: National Snow and Ice Data Center, Boulder, Colorado USA. https://doi.org/10.5067/f6jmovy5navz.
Rignot, E., 1996. Tidal motion, ice velocity and melt rate of Petermann Gletscher, Greenland, measured from radar interferometry. J. Glaciol. 42 (142), 476–485. https://doi.org/10.3189/S0022143000003464.
Rignot, E., Mouginot, J., Scheuchl, B., 2011. Antarctic grounding line mapping from differential satellite radar interferometry. Geophys. Res. Lett.; Washington 38 (1). https://doi.org/10.1029/2011GL047109.
Rignot, E., Ciracì, E., Scheuchl, B., Tolpekin, V., Wollersheim, M., Dow, C., 2024. Widespread seawater intrusions beneath the grounded ice of Thwaites Glacier, West Antarctica. Proceedings of the National Academy of Sciences 121 (22), e2404766121. https://doi.org/10.1073/pnas.2404766121.
Rignot, E., Mouginot, J., Morlighem, M., Seroussi, H., Scheuchl, B., 2014. Widespread, rapid grounding line retreat of Pine Island, Thwaites, Smith, and Kohler glaciers, West Antarctica, from 1992 to 2011. Geophys. Res. Lett. 41 (10), 3502–3509. https://doi.org/10.1002/2014GL060140.
Sandwell, D., Mellors, R., Tong, X., Wei, M., Wessel, P., 2011. Open radar interferometry software for mapping surface deformation. Eos. Trans. AGU 92 (28). https://doi.org/10.1029/2011EO280002.
Scambos, T.A., Bohlander, J.A., Shuman, C.A., Skvarca, P., 2004. Glacier acceleration and thinning after ice shelf collapse in the Larsen B embayment, Antarctica. Geophys. Res. Lett. 31 (18). https://doi.org/10.1029/2004GL020670.
Schmeltz, M., Rignot, E., MacAyeal, D.R., 2001. Ephemeral grounding as a signal of ice-shelf change. J. Glaciol. 47 (156), 71–77. https://doi.org/10.3189/172756501781832502.
Schmidt, B.E., Washam, P., Davis, P.E.D., Nicholls, K.W., Holland, D.M., Lawrence, J.D., Riverman, K.L., Smith, J.A., Spears, A., Dichek, D.J.G., Mullen, A.D., Clyne, E., Yeager, B., Anker, P., Meister, M.R., Hurwitz, B.C., Quartini, E.S., Bryson, F.E., Basinski-Ferris, A., Makinson, K., 2023. Heterogeneous melting near the Thwaites glacier grounding line. Nature 614 (7948), 7948. https://doi.org/10.1038/s41586-022-05691-0.
Schoof, C., 2007. Ice sheet grounding line dynamics: steady states, stability, and hysteresis. J. Geophys. Res. Earth 112 (F3). https://doi.org/10.1029/2006JF000664.
Sergienko, O.V., Wingham, D.J., 2022. Bed topography and marine ice-sheet stability. J. Glaciol. 68 (267), 124–138. https://doi.org/10.1017/jog.2021.79.
Slater, D.A., Straneo, F., Felikson, D., Little, C.M., Goelzer, H., Fettweis, X., Holte, J., 2019. Estimating Greenland tidewater glacier retreat driven by submarine melting. Cryosphere 13 (9), 2489–2509. https://doi.org/10.5194/tc-13-2489-2019.
Slater, D.A., Felikson, D., Straneo, F., Goelzer, H., Little, C.M., Morlighem, M., Fettweis, X., Nowicki, S., 2020. Twenty-first century ocean forcing of the Greenland ice sheet for modelling of sea level contribution. Cryosphere 14 (3), 985–1008. https://doi.org/10.5194/tc-14-985-2020.
Smith, A.M., 1991. The use of tiltmeters to study the dynamics of Antarctic ice-shelf grounding lines. J. Glaciol. 37 (125), 51–58. https://doi.org/10.3189/S0022143000042799.
Sykes, H.J., Murray, T., Luckman, A., 2009. The location of the grounding zone of Evans ice stream, Antarctica, investigated using SAR interferometry and modelling. Ann. Glaciol. 50 (52), 35–40. https://doi.org/10.3189/172756409789624292.
Tsai, V.C., Gudmundsson, G.H., 2015. An improved model for tidally modulated grounding-line migration. J. Glaciol. 61 (226), 216–222. https://doi.org/10.3189/2015JoG14J152.
Van Wychen, W., Davis, J., Burgess, D.O., Copland, L., Gray, L., Sharp, M., Mortimer, C., 2016. Characterizing interannual variability of glacier dynamics and dynamic discharge (1999–2015) for the ice masses of Ellesmere and Axel Heiberg Islands, Nunavut, Canada. J. Geophys. Res. Earth 121 (1), 39–63. https://doi.org/10.1002/2015JF003708.

Van Wychen, W.V., Burgess, D., Kochtitzky, W., Nikolic, N., Copland, L., Gray, L., 2020. RADARSAT-2 derived glacier velocities and dynamic discharge estimates for the Canadian high Arctic: 2015–2020. Can. J. Remote. Sens. 46 (6), 695–714. https://doi.org/10.1080/07038992.2020.1859359.

Vaughan, D.G., 1995. Tidal flexure at ice shelf margins. J. Geophys. Res. Solid Earth 100 (B4), 6213–6224. https://doi.org/10.1029/94JB02467.

Weertman, J., 1974. Stability of the junction of an ice sheet and an ice shelf. J. Glaciol. 13 (67), 3–11. https://doi.org/10.3189/S0022143000023327.

Werner, C., Wegmüller, U., Strozzi, T., Wiesmann, A., 2000. GAMMA SAR and Interferometric Processing Software. ERS - ENVISAT Symposium, Gothenburg, Sweden, pp. 16–20.

White, A., Copland, L., 2018. Area change of glaciers across northern Ellesmere Island, Nunavut, between ~1999 and ~2015. J. Glaciol. 64 (246), 609–623. https://doi.org/10.1017/jog.2018.49.

Wilson, N., Mueller, D., 2023. Radar Tools v. 0.5 [Computer software]. https://doi.org/10.5281/zenodo.439723.

Wilson, N., Straneo, F., Heimbach, P., 2017. Satellite-derived submarine melt rates and mass balance (2011–2015) for Greenland's largest remaining ice tongues. Cryosphere 11 (6), 2773–2782. https://doi.org/10.5194/tc-11-2773-2017.

Wilson, N.J., Flowers, G.E., Mingo, L., 2014. Mapping and interpretation of bed-reflection power from a surge-type polythermal glacier, Yukon, Canada. Ann. Glaciol. 55 (67), 1–8. https://doi.org/10.3189/2014AoG67A101.